

RESEARCH MEMORANDUM

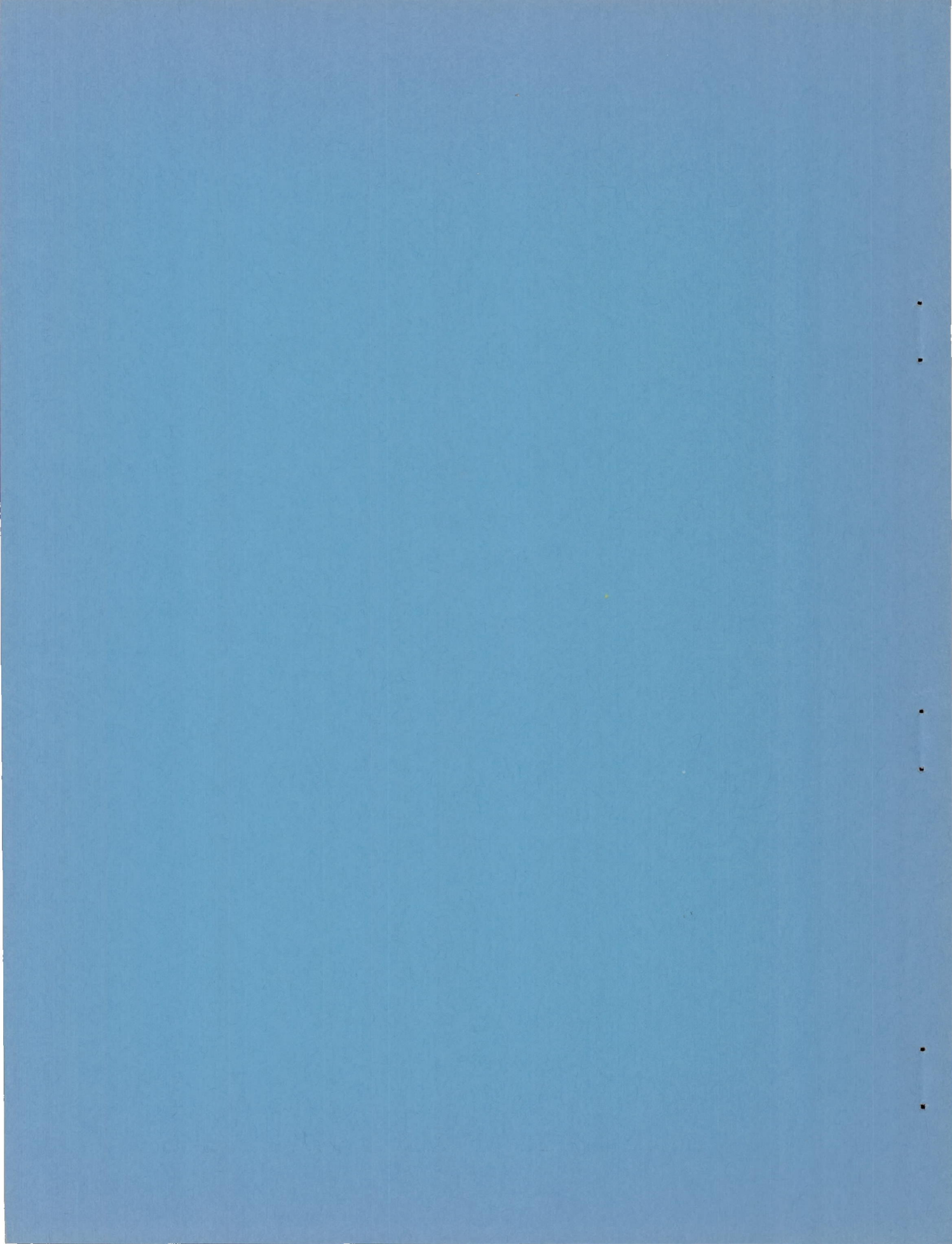
PRELIMINARY INVESTIGATION AT MACH NUMBER 1.9 OF
SIMULATED WING-ROOT INLETS

By Thomas G. Piercy and Maynard I. Weinstein

Lewis Flight Propulsion Laboratory
Cleveland, Ohio

**NATIONAL ADVISORY COMMITTEE
FOR AERONAUTICS
WASHINGTON**

January 19, 1955
Declassified November 14, 1958



NATIONAL ADVISORY COMMITTEE FOR AERONAUTICS

RESEARCH MEMORANDUM

PRELIMINARY INVESTIGATION AT MACH NUMBER 1.9 OF

SIMULATED WING-ROOT INLETS

By Thomas G. Piercy and Maynard I. Weinstein

SUMMARY

An experimental investigation was conducted to study several wing-root inlet configurations at Mach number 1.9. The inlets were of triangular and rectangular shape, and external compression was provided by two-dimensional wedge surfaces. Inlets were tested alternately with straight diffusers of relatively slow diffusion rate and with curved diffusers; the curved-diffuser models simulate the ducting of proposed fighter aircraft requiring relatively short diffusion length and high rates of turning.

The variation of inlet pressure recovery and critical mass flow with angle of attack followed closely the theoretical trends, although the pressure recoveries were considerably lower than predicted by two-dimensional shock theory. Considerably lower pressure recoveries were obtained with the curved subsonic diffusers than with straight diffusers.

Large variations of total pressure and, in some cases, regions of separated flow occurred at the exits of the diffusers. Reductions in the variation of total pressure and elimination of the separated regions were obtained with any of several internal flow-control devices tested with a typical model. However, reduction of the over-all pressure-recovery level generally accompanied improvements in the diffuser-exit total-pressure profiles.

INTRODUCTION

Engine air inlets located in the wing root have shown sufficient merit at subsonic speeds to make them competitive with other inlet locations. Fighter aircraft employing wing-root inlets are currently operational at transonic flight speeds and are being proposed for supersonic velocities.

It has been shown (refs. 1 and 2) that wing-root inlets of the normal-shock type may give satisfactory performance for flight Mach numbers up to 1.5. At higher flight speeds, however, total-pressure losses become excessive and some form of supersonic compression is required.

The present preliminary study was undertaken to explore at Mach number 1.9 the internal flow performance of several possible wing-root inlet designs utilizing two-dimensional external-compression surfaces.

The ducting requirements of proposed fighter aircraft were simulated. Because of length limitations, the subsonic diffusers of this class of aircraft are relatively short and incorporate high rates of turning in order to duct the air to the engine, which is buried within the fuselage. Inlet performance using these curved subsonic diffusers is compared with that obtained with straight diffusers of lower diffusion rate.

Effects on external aerodynamics were not considered; that is, the inlets were tested as nose inlets. However, the effects of inlet side plates simulating a fuselage-boundary-layer splitter plate were determined for most of the configurations.

Additional investigations were also conducted to study the effectiveness of several simple devices designed to improve the diffuser-exit total-pressure profiles of one wing-root inlet model. These tests were conducted in the 18- by 18-inch tunnel of the NACA Lewis laboratory at a Mach number of 1.9.

SYMBOLS

The following symbols are used in this report:

A	area
A_p	projected inlet area at zero angle of attack
l	distance along curved centroidal axis
m_2/m_0	mass-flow ratio, $\rho_2 A_2 V_2 / \rho_0 A_p V_0$
P	total pressure
p	static pressure
q	dynamic pressure, $\frac{1}{2} \rho V^2$

R	radius
V	velocity
x	axial distance
α	angle of attack
ρ	density

Subscripts:

c	choking
cr	critical
max	maximum
0	free stream
1	throat
2	diffuser-exit rake station

APPARATUS AND PROCEDURE

Model Details

Characteristic shapes and dimensions of the wing-root inlets investigated are presented in table I. Four inlet types were studied: Inlet 1 was of triangular shape with supersonic compression provided by an unswept two-dimensional wedge positioned along the upper surface. Inlet 2 was also triangular, but compression was provided with a centrally located unswept wedge. A rectangular cross section was utilized for inlet 3; supersonic compression was obtained from an unswept two-dimensional wedge located along the upper surface. The effect of a compression surface with 40° leading-edge sweepback was investigated with inlet 4, which was also of triangular shape.

Inlets 1, 3, and 4 were tested alternately with straight and curved subsonic diffusers, while inlet 2 was investigated only with a straight diffuser. To distinguish between inlets having the same supersonic-compression surfaces but with alternate subsonic diffusers, the various models have been designated with the letter S or C. For example, model number 4-C represents the 40° swept inlet with curved subsonic diffuser.

Inlet sizing was based on inlet-engine matching considerations; assuming a fixed inlet geometry, inlet throat area was sized to provide a velocity ratio of 1 for a current high-performance engine at a cruise

Mach number of 0.9 and an altitude of 35,000 feet. Wedge compression angles were chosen arbitrarily to provide a compromise between high pressure recovery at Mach number 1.9 and low flow-spillage requirements. The inlets were designed for a theoretical oblique-shock spillage of 2 to 3 percent at Mach number 1.9 and zero angle of attack; as a consequence, an engine bypass (capable of bypassing up to 18-percent mass flow at Mach number 1.9) would be required to minimize spillage drag.

Drawings of the models are presented in figure 1, and model photographs are presented in figure 2. Each model was integrally cast with a mixture of bismuth and tin; however, the leading edges of the inlet were formed from brass inserts in order to maintain the desired sharpness. With each inlet type, transition in the subsonic diffuser was made to a circular cross section. Models 1, 3, and 4 were tested with and without side plates simulating boundary-layer-removal splitter plates.

The lower lips of the triangular inlets were not normal to the free-stream direction. This geometrical feature was the result of maintaining a uniform shock spillage across the width of the inlet. For inlet 2, which incorporates a centrally located compression surface, both upper and lower lips were swept with respect to free-stream direction.

Since the compression surface of inlet 2 is located centrally, this inlet attains maximum pressure recovery when the compression surface is at zero angle of attack with respect to the free stream. The axis of the subsonic diffuser was therefore canted down at 2° (corresponding to a typical cruise angle) so that the maximum pressure recovery could be expected for the cruise condition. For the other inlet types, pressure recovery would be expected to increase with angle of attack.

The area distributions of the inlet subsonic diffusers are presented in figures 3 and 4. For straight-diffuser models (fig. 3), the area distribution near the throat was determined approximately by the criterion that the static-pressure gradient be proportional to the local static pressure (ref. 3). In the more rapidly expanding sections, the area distribution is approximately that given by a 7° -included-angle cone.

For the curved-diffuser models (fig. 4), the total diffusion was less than with the straight diffusers because a centerbody simulating the accessory housing of the engine was included.

Instrumentation

A schematic diagram of the test set-up and model instrumentation is shown in figure 5. As indicated in figure 5(a), the model was hung from a vertical support strut with which the model angle of attack was

varied from -3° to 9° . The aft support body contained four static-pressure orifices which were used for determining inlet mass flow. The forward support body contained the total-pressure rakes used in determining the inlet total-pressure recovery. Since the curved-diffuser models were somewhat shorter than the corresponding straight models, two forward support bodies were used. The lengths of these sections (figs. 5(b) and (c)) were chosen so that each inlet was at approximately the same station in the tunnel test section. The forward support body for the curved-diffuser models also housed the strut for support of the curved-diffuser accessory housing. Over-all total-pressure recovery was obtained from the area-weighted average of measurements at the diffuser exit. Inlet mass flow was determined using the static orifices in the aft support body together with the assumption of a choked exit, the area of which was controlled with a remotely operated plug.

Flow conditions near the throats of inlets 1, 3, and 4 were determined with the rakes indicated in figure 6. In addition, static orifices were located on the supersonic compression surfaces and throughout the subsonic diffuser of each model.

The effects of rods and screens (see fig. 7) placed internally in the subsonic diffuser as a means of improving the exit total-pressure profiles of model 3-S were investigated briefly.

For the tests at Mach number 1.9, tunnel total pressure was approximately atmospheric while total temperature was held at 150° F. The resulting Reynolds number was about 3.25×10^6 per foot. The dew point was maintained below -10° F to minimize condensation effects.

Data were also obtained for zero flight speed conditions by induction of ambient air through each inlet. Instrumentation for these tests was identical to that for the tests at Mach number 1.9 except that inlet mass flow was determined with a standard A.S.M.E. orifice connected downstream of the inlet rake station.

DISCUSSION OF RESULTS

Pressure-Recovery and Mass-Flow Data

Inlet performance data for the angle-of-attack range of -3° to 9° are presented in figure 8 for each wing-root inlet model investigated. Inlet mass flow is referenced to that which would pass through the stream tube of the projected inlet capture area at zero angle of attack. As a result, the critical inlet mass-flow ratio increased with angle of attack because of the increase in inlet projected area. Arrows on the mass-flow scale indicate the theoretical critical values based on two-dimensional shock theory.

The measured critical mass flow at zero angle of attack was generally 2 to 4 percent lower than the design value, except for model 2-S for which the mass flow was about 3 percent larger than expected. These differences are probably due, in large measure, to fabrication tolerances in the inlet capture area. Nevertheless, the variation of measured critical mass-flow ratio with angle of attack followed the trends predicted. For the swept inlets, two-dimensional analysis of the normal component flow indicates that detachment of the flow at the compression surface should occur at angles of attack greater than 3° . In view of the difficulties encountered in predicting shock locations and flow directions for detached flow conditions, the arrows on the mass-flow scale for the swept inlets merely indicate the ratio of projected inlet area at angle of attack to that at zero angle of attack.

The inlets showed little or no subcritical stability. (The only stability noted occurred with the straight-diffuser models 1-S and 3-S at the highest angles of attack investigated.) In general, it was difficult to interpret the inlet shock patterns with existing tunnel schlieren equipment because of the skewed nature of the inlet compression surfaces. Shock instability noted in the schlieren equipment has been designated by dashed lines in figure 8. Quite often minor shock oscillation was observed for mass-flow ratios less than the critical value; when the mass flow was reduced below the peak pressure value, the shock oscillation appeared to increase in both frequency and amplitude.

These general observations were later verified by the installation of a dynamic-pressure pickup with model 4-S. With this instrumentation a small-amplitude pressure variation ($\Delta p_2/P_0$ of 0.03) was observed during supercritical operation. (This fluctuation is probably due to local boundary-layer separation within the inlet.) For angles of attack of 3° or less, no change in this pressure fluctuation was noted as the mass flow was reduced to the peak pressure-recovery value. For lower mass flows, however, the pressure fluctuation increased rapidly to $\Delta p_2/P_0$ of 0.15. At angles of attack of 6° and 9° , the pressure fluctuation remained at $\Delta p_2/P_0$ of 0.03 throughout the mass-flow range investigated.

For the straight-diffuser inlets (with the exception of model 2-S), peak pressure recovery generally was obtained at mass flows within 5 percent of the critical values; with the curved-diffuser models, peak pressure recovery occurred at lower mass flows (up to 17 percent less than the critical mass flow for model 4-C).

Effect of Inlet Side Plates and Curved Diffusers

The effect of inlet side plates on inlet peak pressure recovery has been summarized in figure 9. The unswept inlets were benefited

slightly by the use of the side plates, whereas the swept inlet experienced a total-pressure loss of approximately 0.02. An examination of figure 8 shows little or no effect of side plates on the critical inlet mass flow. Inasmuch as the side plate for each model was aligned with the local free-stream direction, all noted changes in performance are believed due to the effects of side-plate boundary-layer growth on the subsonic-diffuser performance.

The experimental pressure recovery of each inlet type is compared with a two-dimensional theoretical shock pressure recovery in figure 10. The theoretical recoveries were computed from the losses across the oblique shock originating at the compression surface and across an internal normal shock at the throat section of the model. For the swept inlets, detachment of the normal flow component complicated the analysis. The theoretical pressure recovery presented in figure 10 for the swept inlets is based on the streamwise flow plane rather than the normal flow component. Experimental values of critical and peak pressure recovery are summarized for both straight and curved diffusers.

The experimental pressure recovery follows the theoretical trends with angle of attack fairly closely although at lower values, indicating considerable diffusion losses. At the critical inlet pressure-recovery condition, the losses were considerably larger for the curved-diffuser models than for comparable straight-diffuser models utilizing the same supersonic-compression surfaces.

The effects of inlet shape, compression-surface sweep, and compression-surface location may also be obtained from figure 10. With the exception of the inlet with centrally located compression surface, a peak pressure recovery of 85.3±1 percent was attained; also, diffusion losses were essentially the same regardless of inlet shape or compression-surface sweep. However, the minimum diffusion loss for the centrally located compression-surface inlet was larger than for the other straight-diffuser inlet types.

At zero angle of attack the pressure recovery of the swept inlet is somewhat lower than was attained with either the triangular or rectangular inlets of zero leading-edge sweep, probably because of the relatively small amount of compression offered by the swept inlets. The swept inlets could probably have been made comparable to the unswept inlets at low angles of attack by using larger compression angles.

Exit and Inlet Total-Pressure Distributions

Total-pressure profiles and wall static-pressure ratios at the diffuser exits are presented in figure 11 for angles of attack of zero and 6°. These distributions correspond to operation at or near

the peak pressure-recovery condition. The projected inlet throat section is also shown with dashed lines for each inlet type to indicate the direction and rate of subsonic diffusion. Separation, when it occurred at the exit-rake station, is indicated with a series of parallel shaded lines.

For all inlets large total-pressure gradients occurred across the exit of the diffuser. At zero angle of attack the minimum spread of total-pressure recovery (± 8 percent of the weighted average total pressure) occurred with model 2-S. For the other straight-diffuser models, variations of from -13 to +19 percent were observed. Even larger variations of total pressure (up to ± 28 percent) occurred in the curved diffusers. At an angle of attack of 6° , the over-all pressure variation across the diffuser exit was generally reduced.

For the straight-diffuser models the maximum pressure region was usually in the lower quadrants, with separation (when it occurred) in the upper quadrants. For the curved-diffuser models the high-pressure regions occurred on the windward side of the simulated accessory housing, while relatively low pressure was measured on the leeward side of the housing. Separation was observed on both the windward diffuser wall and on the leeward accessory-housing side at zero angle of attack; however, no separation was evident at 6° . The largest separated regions occurred with model 3-S, probably because of the rapid turning of the upper diffuser wall downstream of the throat. Roughness added upstream of the throat did not decrease the separation, but lowered the average total-pressure recovery.

The static pressure at the exit station of the straight diffusers was quite uniform, whereas circumferential static-pressure gradients were frequently measured with the curved diffusers. Mach number or velocity profiles at the exits of the straight diffusers may be obtained quite easily from the static- and total-pressure ratios presented. However, for the curved diffusers it would be necessary to account for the circumferential static-pressure variation in determining the values of local static- to total-pressure ratios.

Typical total-pressure distributions and wall static-pressure ratios near the throats of several models during subcritical inlet operation are presented in figure 12. These data were obtained with the inlet rakes of figure 6. The distributions were obtained with the straight-diffuser models, but apply equally well to the comparable curved-diffuser models inasmuch as the same supersonic-compression surfaces were used. The pressure recovery obtained from two-dimensional shock theory is presented for each condition.

Separation at the inlet throat was observed only for the swept inlets. This separation occurred in the upper corner of the inlet at

the junction of compression surface and inlet side wall and was increased by the addition of the side plate. Low total pressures existed along the upper throat surfaces and inlet side wall because of boundary-layer growth on these surfaces. The highest pressures in general occurred near the centroids of the inlet cross section. The local regions where measured pressures were higher than predicted by the two-dimensional shock theory were probably caused by shock patterns different from those assumed; that is, boundary-layer growth in the supersonic diffuser may have caused local oblique shocks not accounted for.

Supersonic and subsonic diffusion in the various models may be further evaluated by means of static-pressure distributions on the compression surfaces and throughout the subsonic diffuser. Typical plots of these static-pressure distributions and corresponding exit total pressures are given in figure 13 for critical inlet operation. The outlines shown correspond to plan forms of the inlets. Solid internal lines correspond to the intersection of constant pressure surfaces on the internal upper surface of the model, while the dashed internal lines are for the internal lower surface of the model.

The theoretical static-pressure ratios on the compression surfaces were 0.28, 0.38, and 0.22 for inlets 1, 3, and 4, respectively. The measured static pressures on the compression surfaces were reasonably close to the theoretical values, and the pressures for comparable straight- and curved-diffuser models were about equivalent, as was expected. The better diffuser performance of the straight diffusers is evident from comparisons of the static-pressure gradients and the total-pressure profiles at the diffuser exit. The static pressure in the curved models first increased in the axial direction and then decreased, indicating a reacceleration of the flow. By comparison, the static pressure continually increased in the straight diffuser. The static pressure also varied around the diffuser periphery for the curved diffusers, whereas it appeared to be uniform for the straight diffusers.

Improvement of Exit Total-Pressure Profiles

Several internal-flow devices for improvement of the exit total-pressure profiles were investigated. Model 3-S, which had exhibited an undue amount of separation, was selected for these tests. The control devices investigated are presented in figure 7 and included full and half screens of 0.5-inch mesh and 0.051-inch diameter located at model station 9.0, which was approximately $2\frac{1}{2}$ inches forward of the exit total-pressure rake. Also investigated were 1/8-inch-diameter rods inserted through the lower half of the diffuser. The area blockage of the three devices was approximately 21, 11, and 8 percent, respectively.

With the measured subsonic-diffuser losses of figure 10 accounted for, the average Mach number of the flow approaching the flow devices for critical inlet operation was computed to be approximately 0.38.

The inlet pressure-recovery and mass-flow characteristics with each flow device are presented in figure 14. Insertion of the flow devices into the diffusers had little effect on inlet supercritical mass flow but decreased both critical and peak pressure recovery. Changes in pressure-recovery performance are most easily observed in figure 15, where peak and critical total-pressure recoveries with the flow devices are summarized and compared with the original inlet with no internal-flow device. The largest loss of pressure recovery was incurred when the full screen was used. These losses were substantially reduced when the screen was used only in the lower half of the diffuser. The minimum loss of pressure recovery occurred when the rods were inserted in the lower diffuser half. As indicated in figure 15, small pressure-recovery improvements were noted in the intermediate angle-of-attack range.

The total-pressure loss across the screens, expressed as a fraction of the local dynamic pressure, is presented in figure 16. Also presented for comparison are the pressure-loss data of reference 4, which were obtained with uniform flow approaching full screens; the data selected for comparison correspond to full screens having the area blockages considered herein. Since the pressure losses varied with angle of attack and the minimum loss was larger than might be predicted from reference 4, it is indicated that (1) the losses across the screens (or other flow-straightening devices) are probably a function of the velocity profile approaching the screens, and (2) pressure-loss data obtained with uniform flow can not be used to predict the losses when the flow is not uniform.

The resulting total-pressure profiles at the exit of the diffuser are presented in figures 17 and 18 for angles of attack of zero and 6° and are compared with the original profiles. Each flow-control device eliminated the separation over the upper half of the diffuser exit and reduced the spread between high and low pressures. The variation of total pressure at the exit station for zero angle of attack was approximately ± 8 , ± 5 , and ± 15 percent of the weighted average total pressure for the full-screen, half-screen, and rod devices, respectively. These values compare with -13 to 18-percent variation for the original pressure distribution. At an angle of attack of 6° further decreases in pressure spread were obtained except with the half-screen device, which yielded a spread of -4 to 9 percent. Therefore, the full-screen method generally offered better exit profiles than did either the half-screen or rod method, especially at angles of attack other than zero; however, it was also noted that the largest loss of total pressure was incurred with the full screen. The relative merits of these three methods for internal control of exit total-pressure profiles in an actual installation would depend upon the allowable total-pressure recovery and also upon the limits of total-pressure variation across the compressor face of the turbojet engine.

Inlet Tests at Zero Flight Speed

Take-off conditions at zero flight speed were evaluated by induction of ambient air through the inlets with tunnel exhauster equipment. The resulting pressure-recovery and mass-flow data are presented in figure 19. Mass flow through the inlets is referenced to the theoretical choking mass flow determined from the minimum throat area and the ambient total pressure. Also presented for comparison is the theoretical performance of an open-nose sharp-lip inlet (ref. 5). The performance of all inlets was reasonably close to the theoretical values (which included an assumed subsonic-diffuser loss of 5 percent of the inlet dynamic pressure), although the pressure recovery was generally lower than theoretical. Each inlet attained within 0.03 of the theoretical mass-flow ratio.

SUMMARY OF RESULTS

A preliminary investigation was conducted at Mach number 1.9 to study the internal performance of several wing-root inlets using two-dimensional external-compression surfaces. Parameters studied included inlet shape, sweep of the compression-surface leading edge, and compression-surface location. The inlets were tested with relatively short curved subsonic diffusers, simulating the ducting requirements of proposed fighter aircraft, and with straight diffusers of lower diffusion rate. The results of this investigation may be summarized as follows:

1. The variation of inlet total-pressure recovery and mass flow with angle of attack followed the trends predicted by theory, although the pressure recovery for each inlet type was lower than the theoretical values. The diffusion losses were essentially independent of inlet shape and sweep of the compression-surface leading edge. Somewhat larger losses were incurred when the compression surface was located centrally compared with the upper leading-edge location for a triangular-shaped inlet.
2. Inlets with curved subsonic diffusers suffered considerably larger diffusion losses than were incurred with straight diffusers.
3. Variations in total-pressure recovery across the diffuser exit were as large as ± 28 percent of the weighted average pressure for the curved-diffuser models compared with 19 percent for the straight-diffuser models. Separation at the exit frequently occurred. Several internal-flow-control devices were installed in a typical inlet; these devices

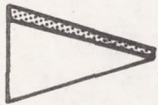
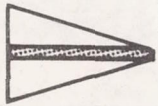
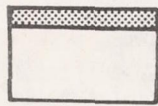
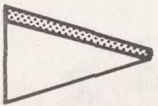
eliminated the separated regions and reduced the variation of pressure recovery across the diffuser exit. However, improvement in exit profile was accompanied by a loss in over-all total-pressure recovery. These losses could not be predicted from data which had been obtained with uniform flow approaching the flow-control devices.

Lewis Flight Propulsion Laboratory
National Advisory Committee for Aeronautics
Cleveland, Ohio, September 24, 1954

REFERENCES

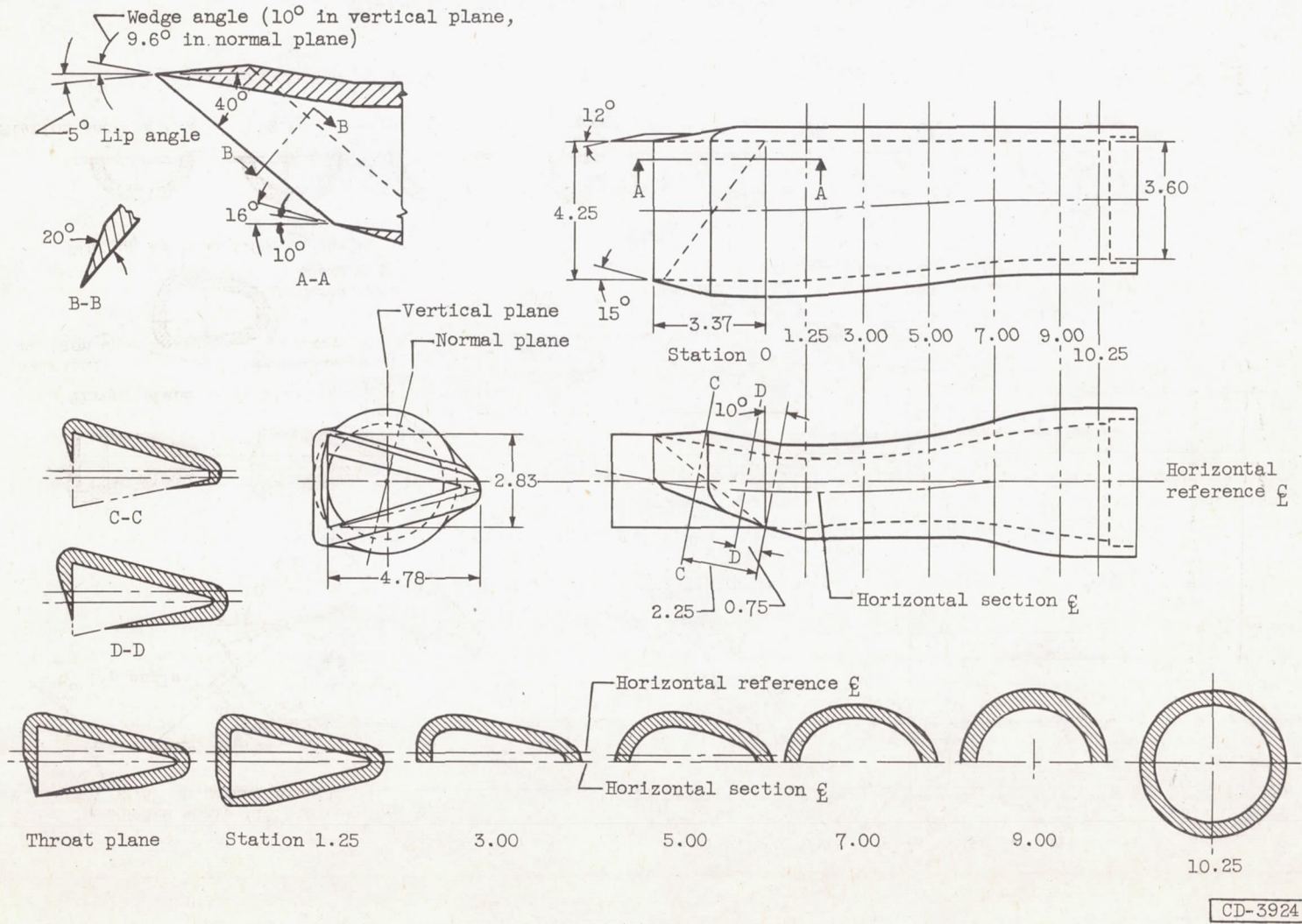
1. Howell, Robert R., and Keith, Arvid L., Jr.: An Investigation at Transonic Speeds of the Aerodynamic Characteristics of an Air Inlet Installed in the Root of a 45° Sweptback Wing. NACA RM L52H08a, 1952.
2. Howell, Robert R., and Trescot, Charles D., Jr.: Investigation at Transonic Speeds of Aerodynamic Characteristics of a Semielliptical Air Inlet in the Root of a 45° Sweptback Wing. NACA RM L53J22a, 1953.
3. Davis, Wallace F., Edwards, Sherman S., and Brajnikoff, George B.: Experimental Investigations at Supersonic Speeds of Twin-Scoop Duct Inlets of Equal Area. IV - Some Effects of Internal Duct Shape upon an Inlet Enclosing 37.2 Percent of the Forebody Circumference. NACA RM A9A31, 1949.
4. Adler, Alfred A.: Variation with Mach Number of Static and Total Pressures Through Various Screens. NACA WR L-23, 1946. (Supersedes NACA CB L5F28.)
5. Fradenburgh, Evan A., and Wyatt, DeMarquis D.: Theoretical Performance Characteristics of Sharp-Lip Inlets at Subsonic Speeds. NACA TN 3004, 1953.

TABLE I. - MODEL CHARACTERISTICS

Model	Inlet	Inlet shape	Sweep angle of wedge, deg	Compression-surface location	Subsonic-diffuser type	Wedge angle, ^a deg	Projected frontal area at zero angle of attack, sq in.	Throat area, sq in.
1-S	1		0	Upper	Straight	9.6	6.68	5.19
1-C					Curved			
2-S	2		0	Center	Straight	10	6.68	5.19
3-S	3		0	Upper	Straight	12	6.95	5.19
3-C					Curved			
4-S	4		^b 40.0	Upper	Straight	6.0	6.31	5.19
4-C					Curved			

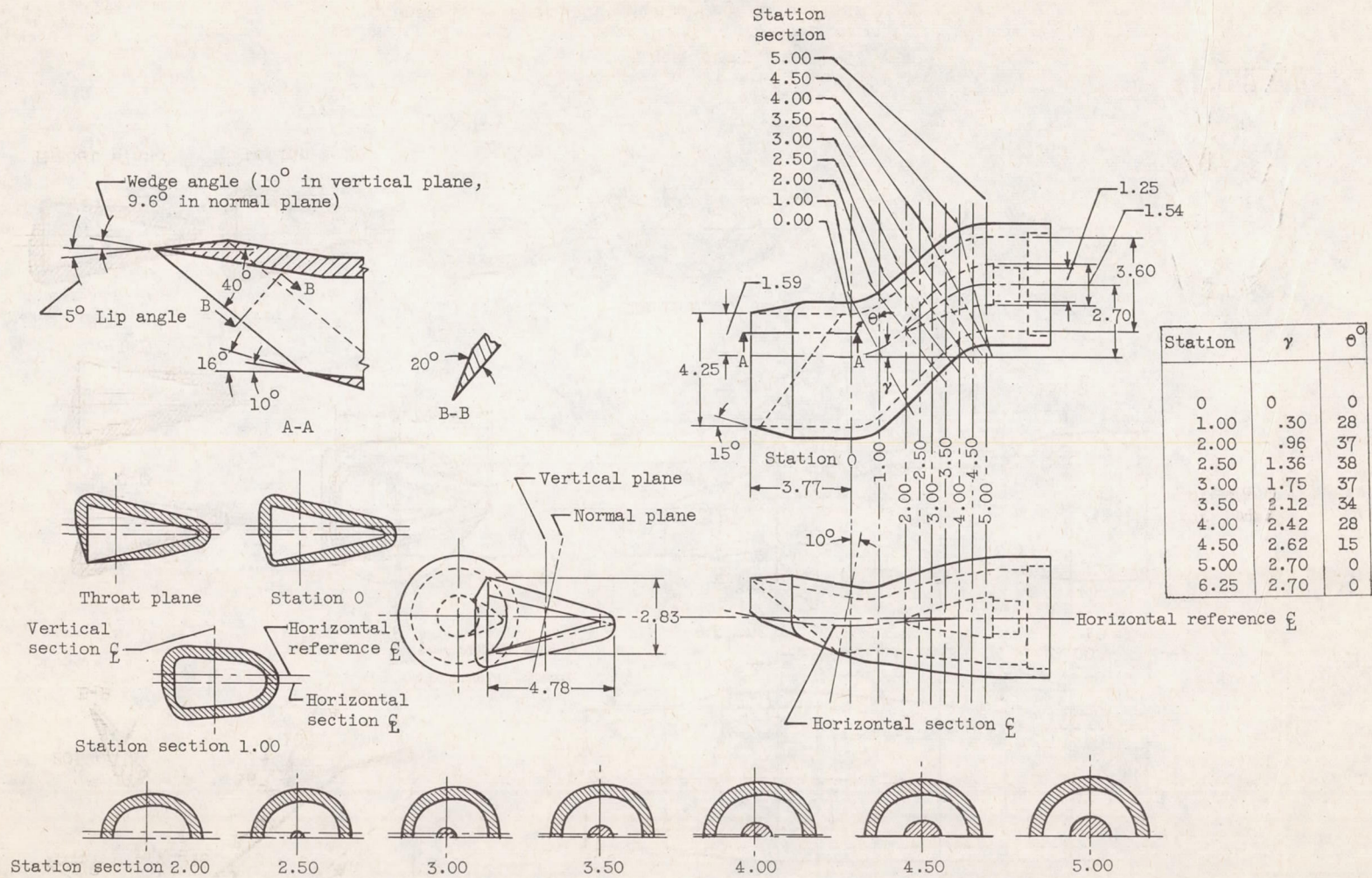
^aMeasured in stream direction in plane normal to wedge leading edge.

^bIn plan view, 40.0°; with respect to air flow, 38.8°.



(a) Model 1-S.

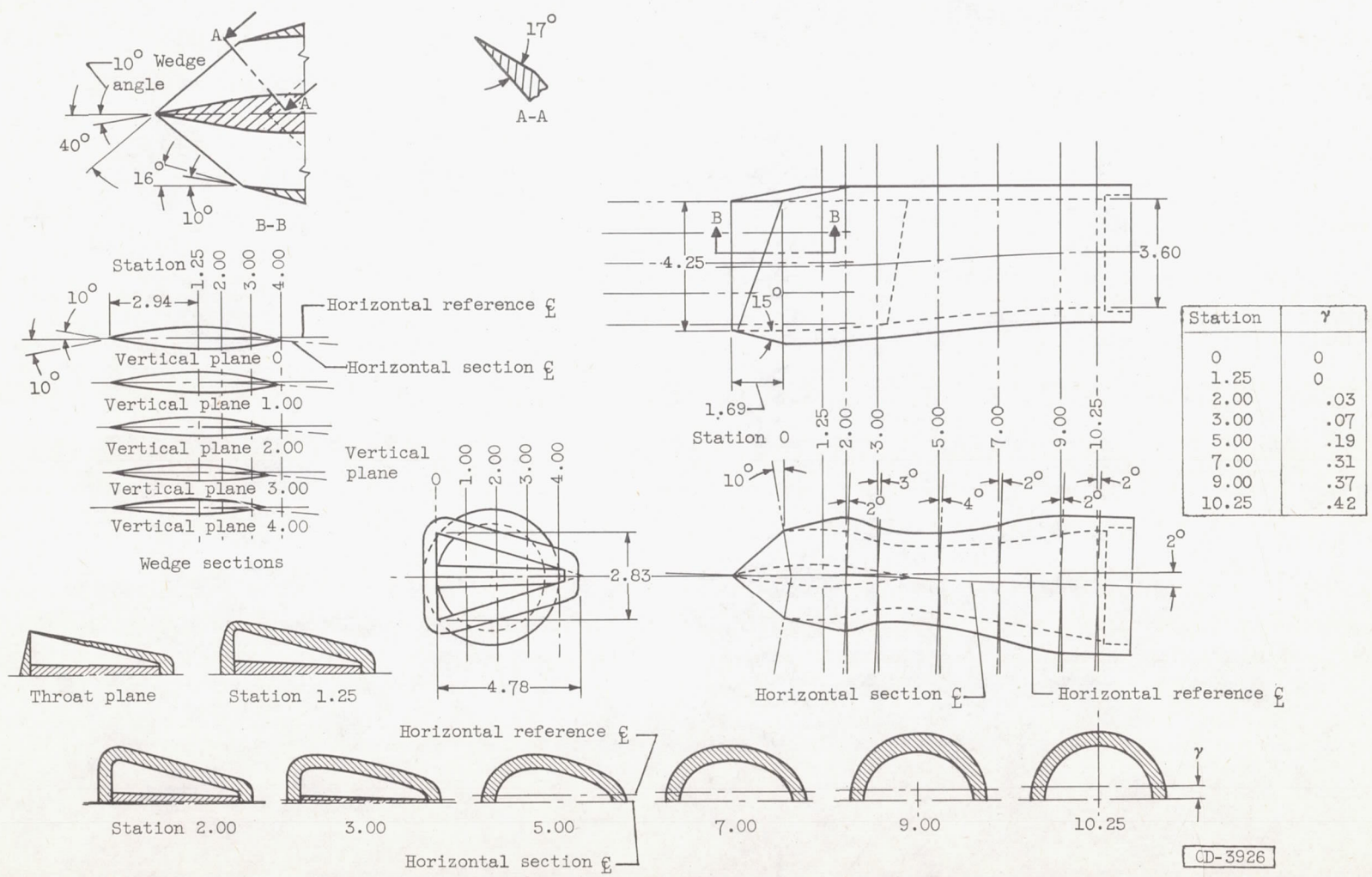
Figure 1. - Sketch of models (all dimensions in inches).



CD-3925

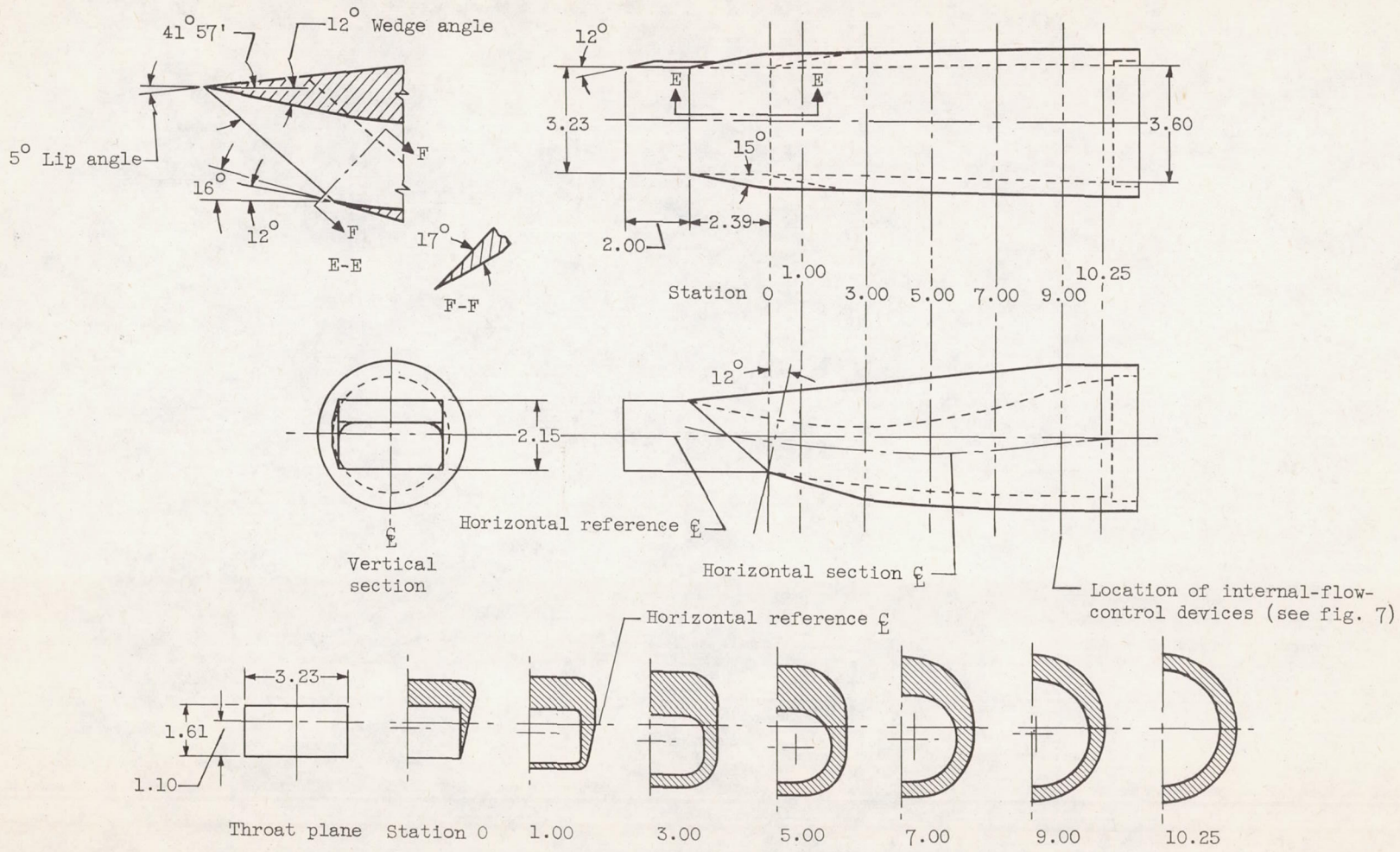
(b) Model 1-C.

Figure 1. - Continued. Sketch of models (all dimensions in inches).



(c) Model 2-S.

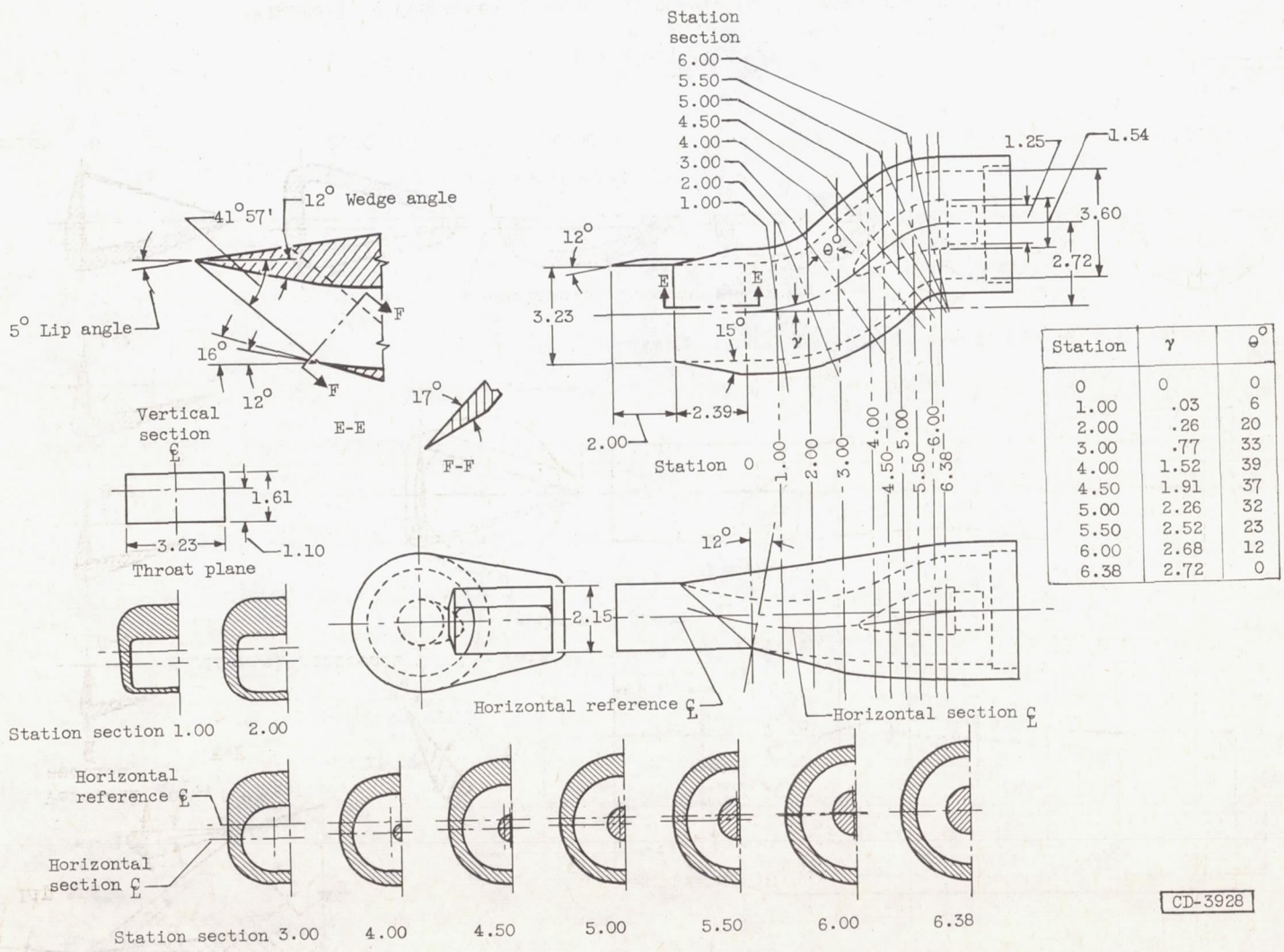
Figure 1. - Continued. Sketch of models (all dimensions in inches).



CD-3927

(d) Model 3-S.

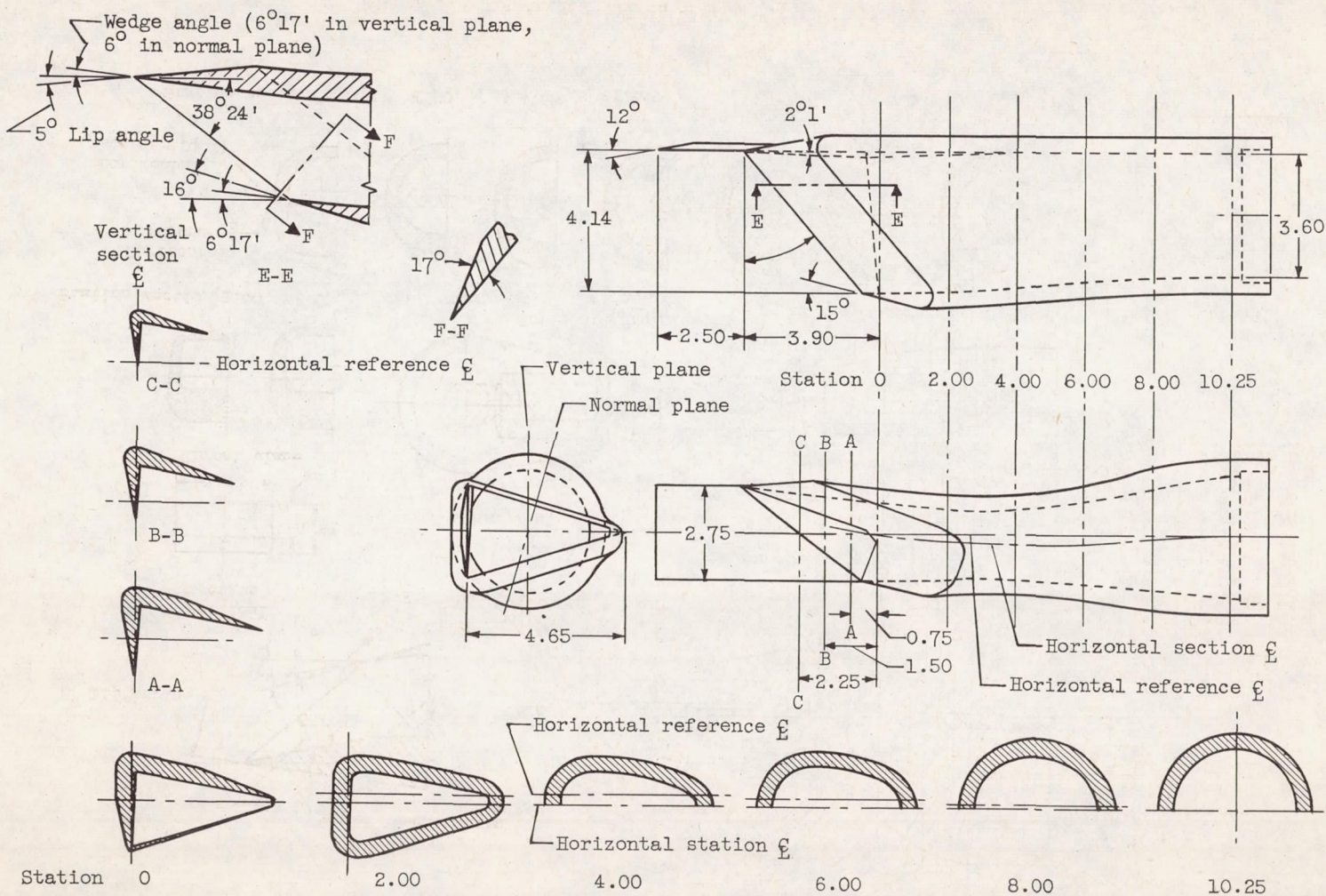
Figure 1. - Continued. Sketch of models (all dimensions in inches).



(e) Model 3-C.

Figure 1. - Continued. Sketch of models (all dimensions in inches).

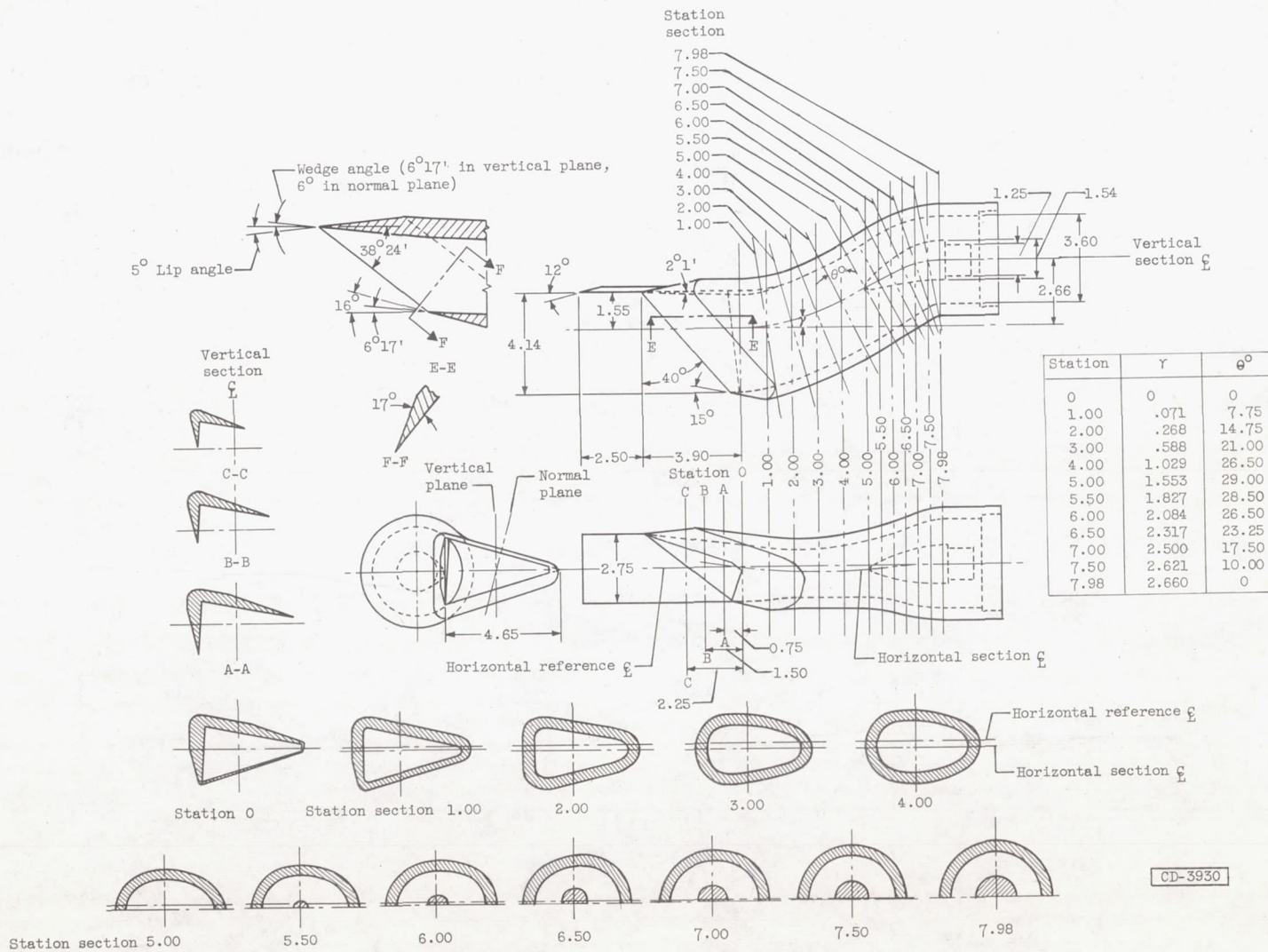
CD-3928



(f) Model 4-S.

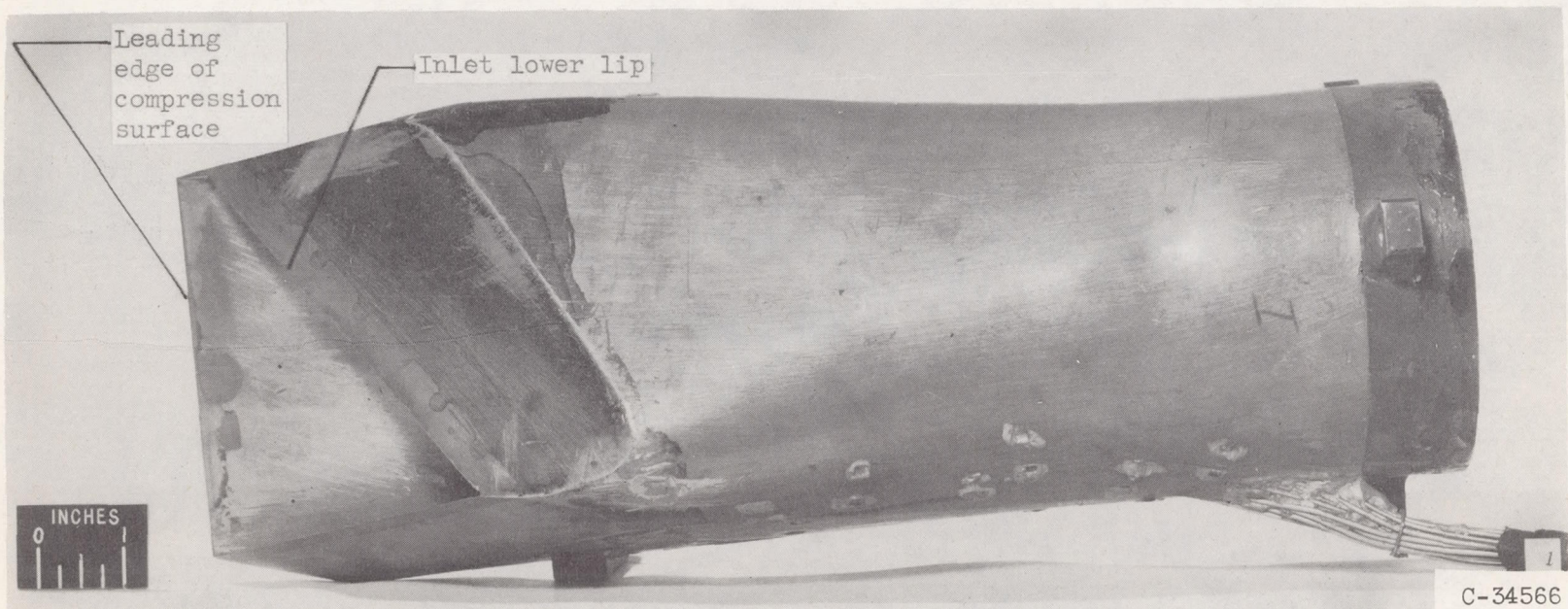
CD-3929

Figure 1. - Continued. Sketch of models (all dimensions in inches).



(g) Model 4-C.

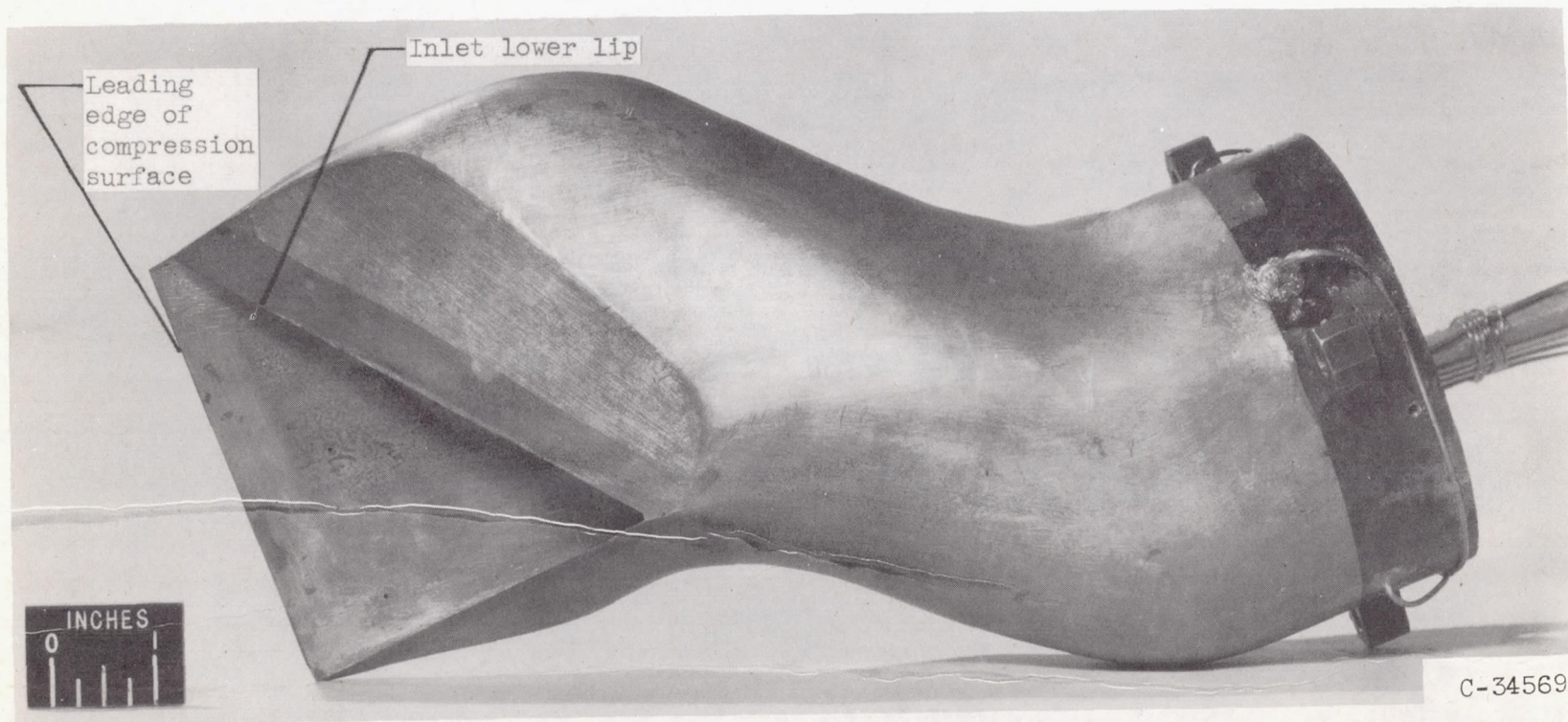
Figure 1. - Concluded. Sketch of models (all dimensions in inches).



View of lower side of model

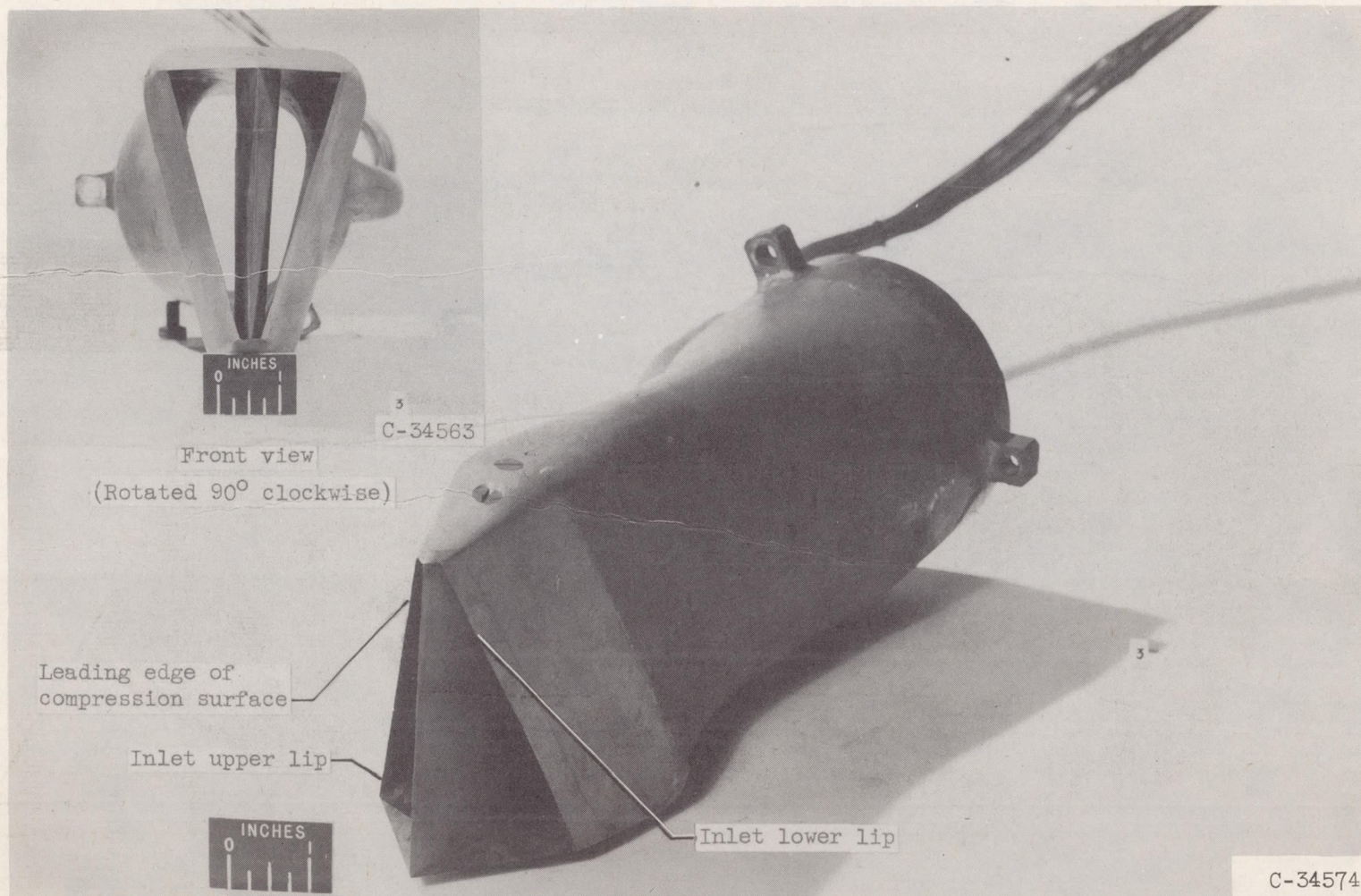
(a) Model 1-S.

Figure 2. - Photographs of wing-root inlet models.



(b) Model 1-C.

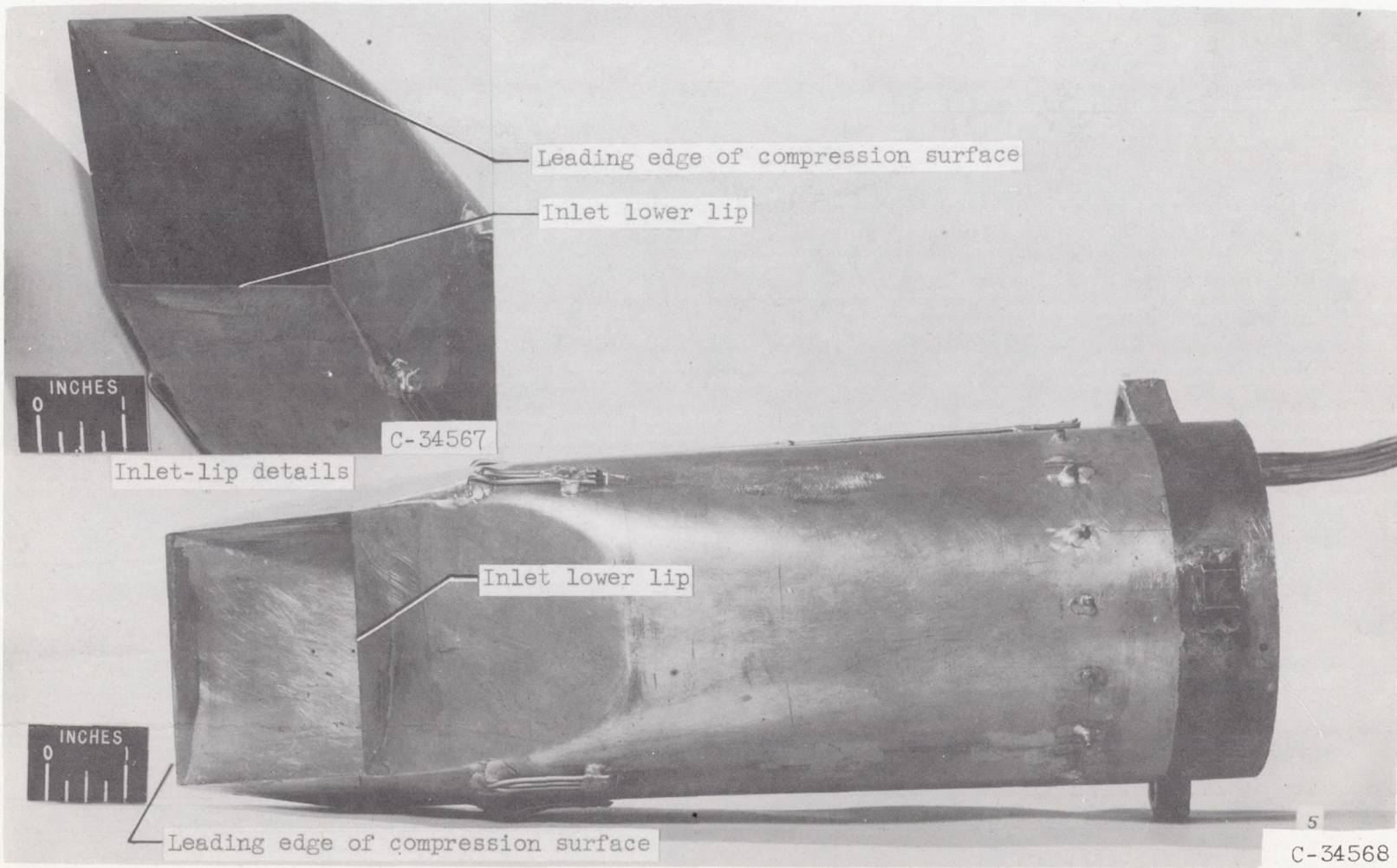
Figure 2. - Continued. Photographs of wing-root inlet models.



One-fourth lower front view

(c) Model 2-S.

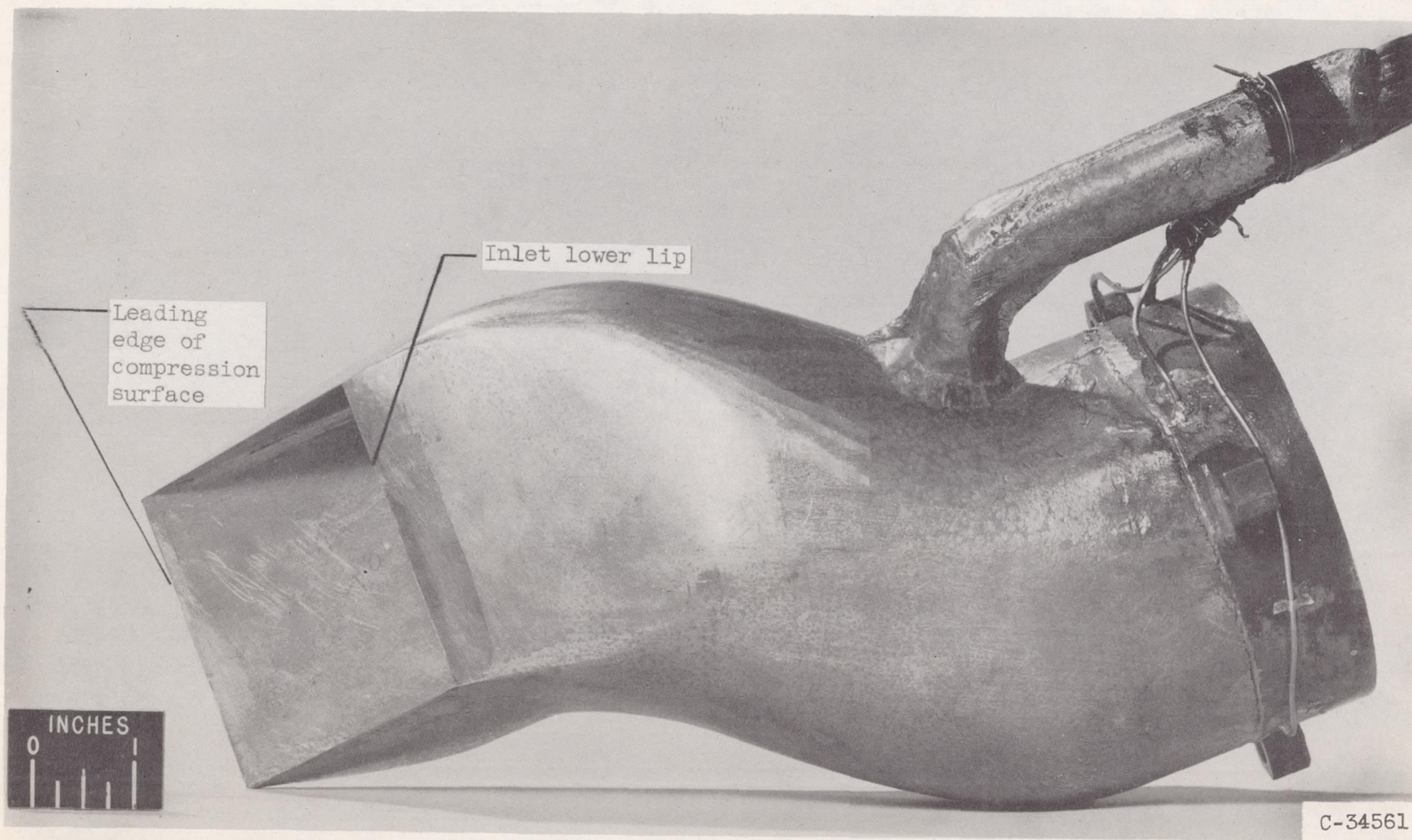
Figure 2. - Continued. Photographs of wing-root inlet models.



View of lower side of model

(d) Model 3-S.

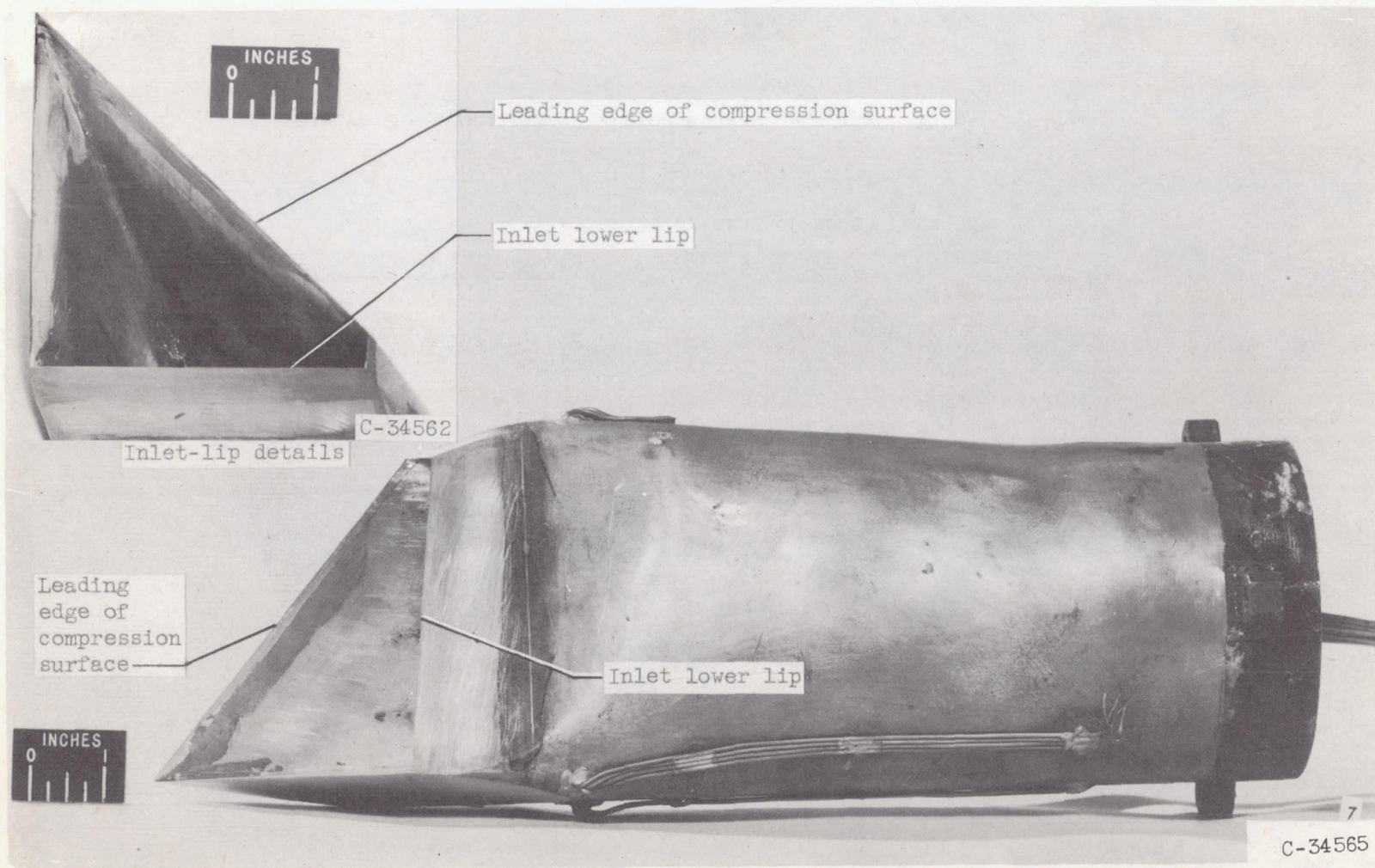
Figure 2. - Continued. Photographs of wing-root inlet models.



View of lower side of model

(e) Model 3-C.

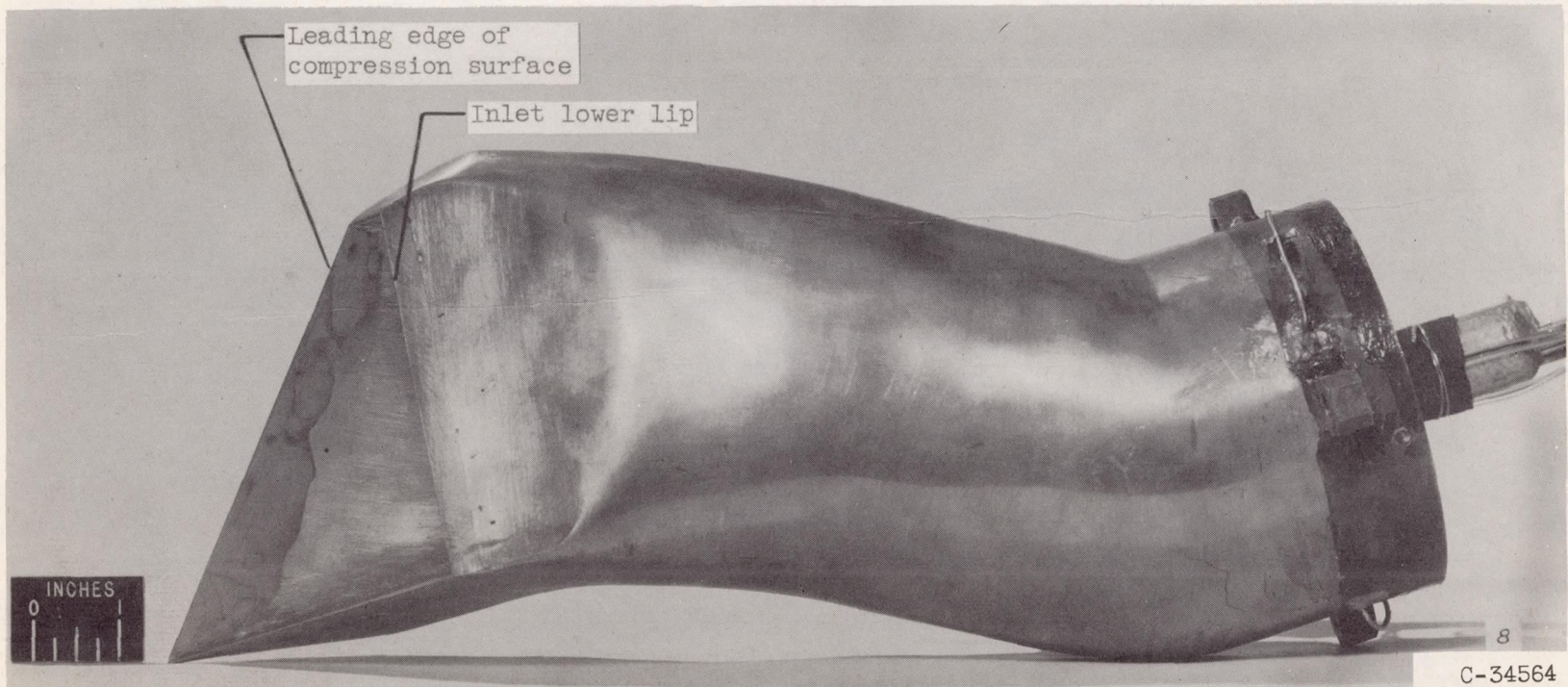
Figure 2. - Continued. Photographs of wing-root inlet models.



View of lower side of model

(f) Model 4-S.

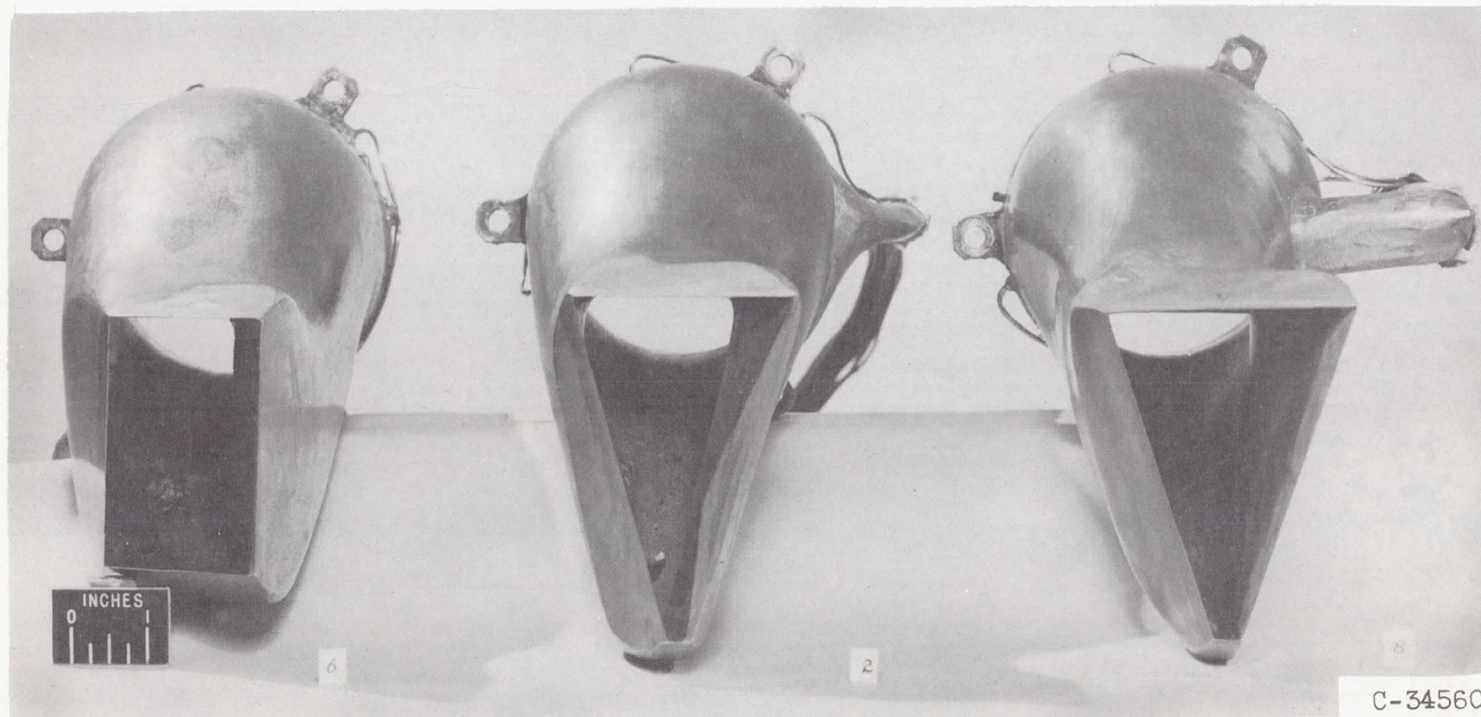
Figure 2. - Continued. Photographs of wing-root inlet models.



View of lower side of model

(g) Model 4-C.

Figure 2. - Continued. Photographs of wing-root inlet models.



Front view of curved-diffuser models
(Models rotated 90° clockwise)

(h) Model 3-C.

(i) Model 1-C.

(j) Model 4-C.

Figure 2. - Concluded. Photographs of wing-root inlet models.

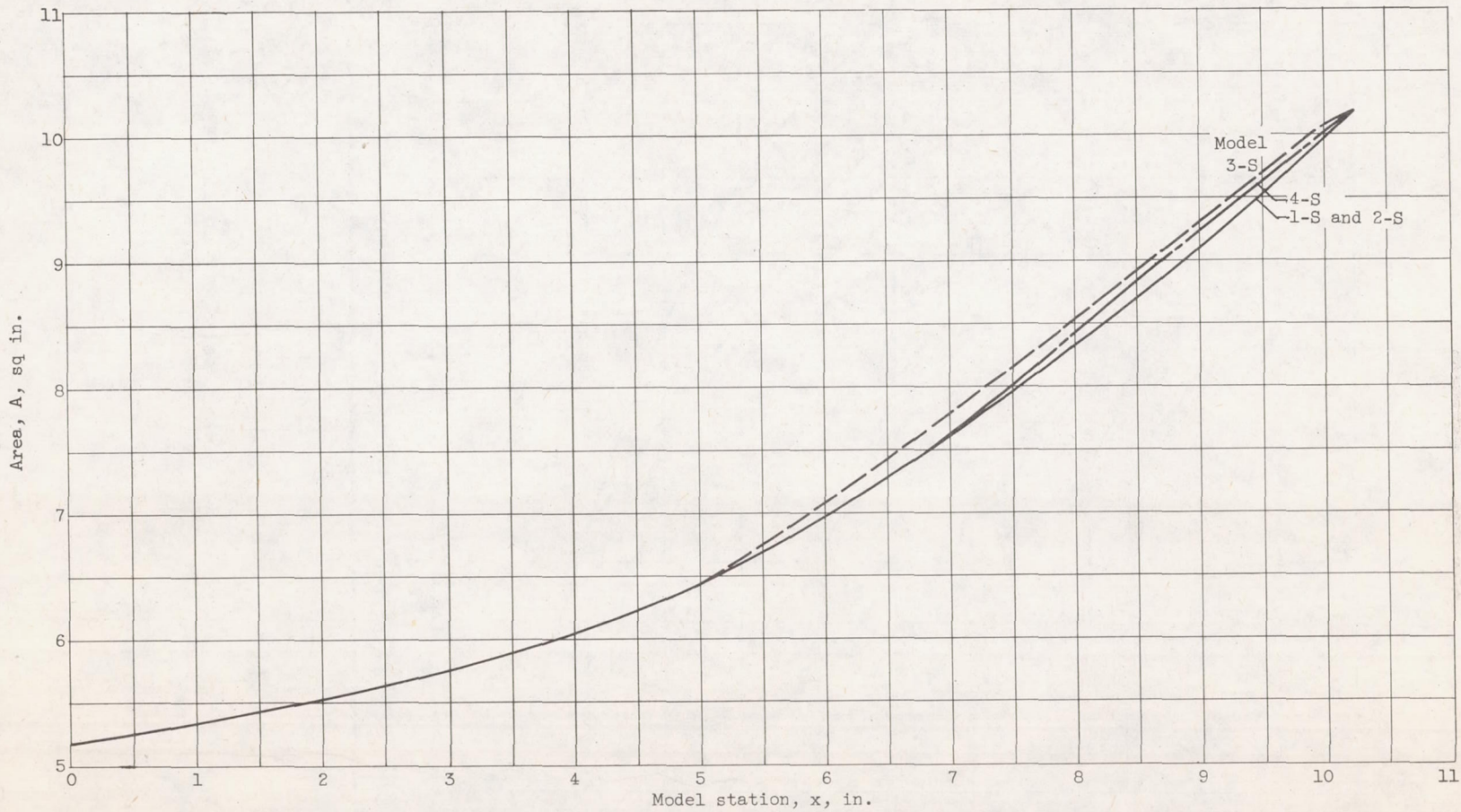
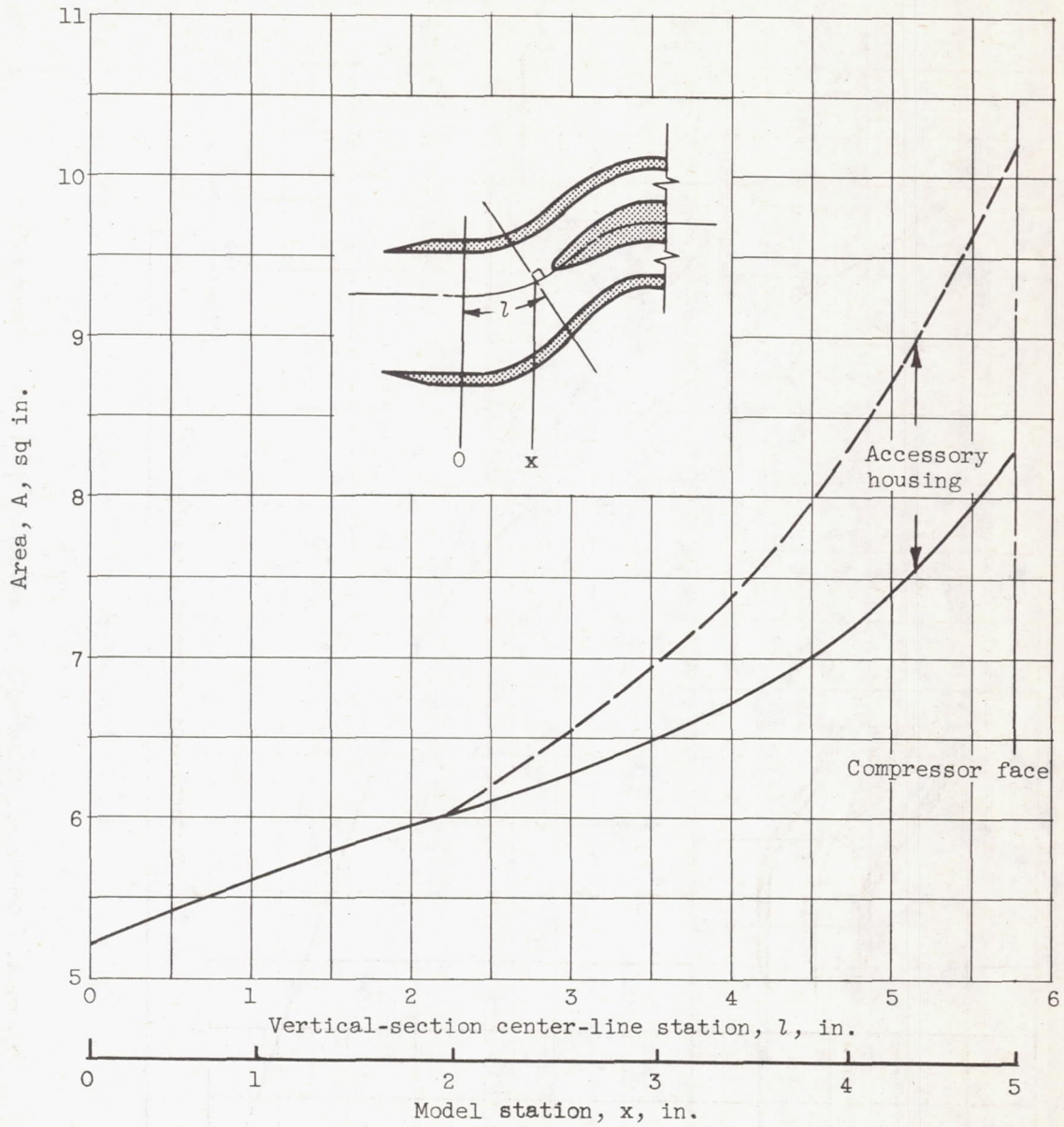
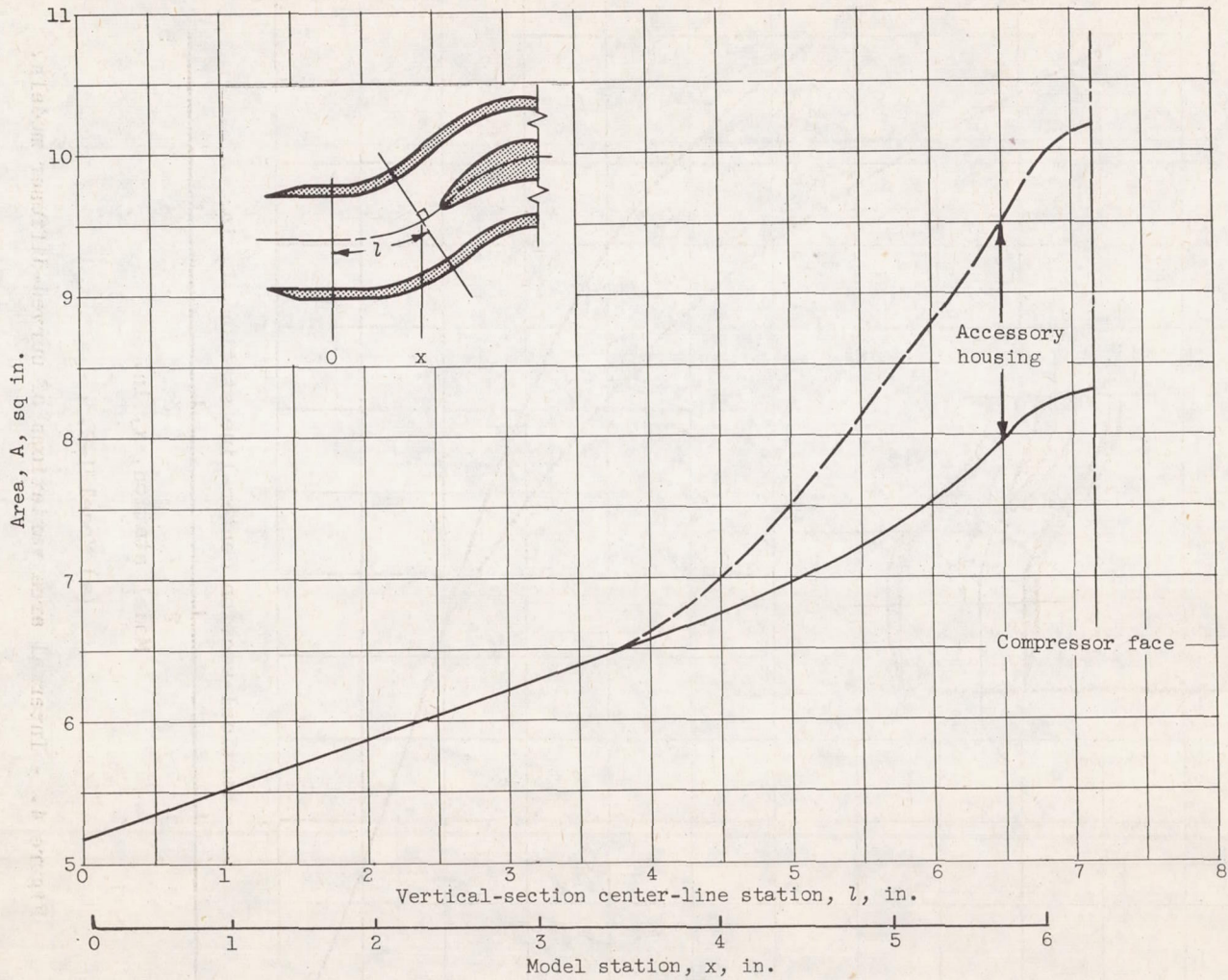


Figure 3. - Internal area variation for straight-diffuser models.



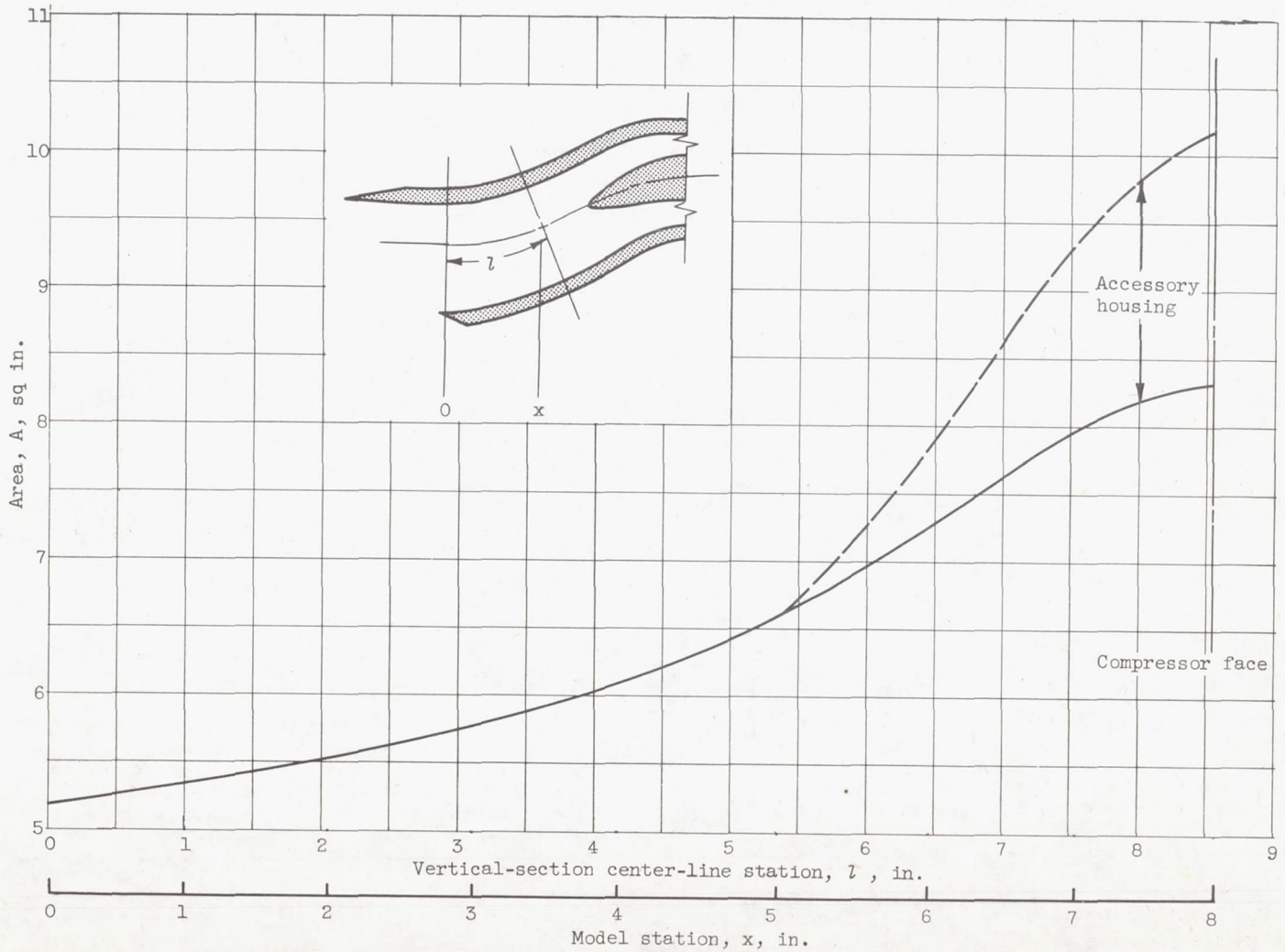
(a) Model 1-C.

Figure 4. - Internal area variations of curved-diffuser models.



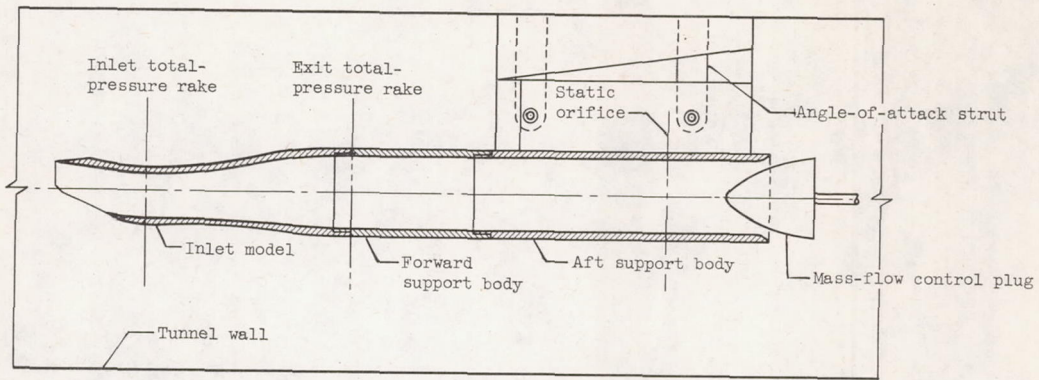
(b) Model 3-C.

Figure 4. - Continued. Internal area variations of curved-diffuser models.

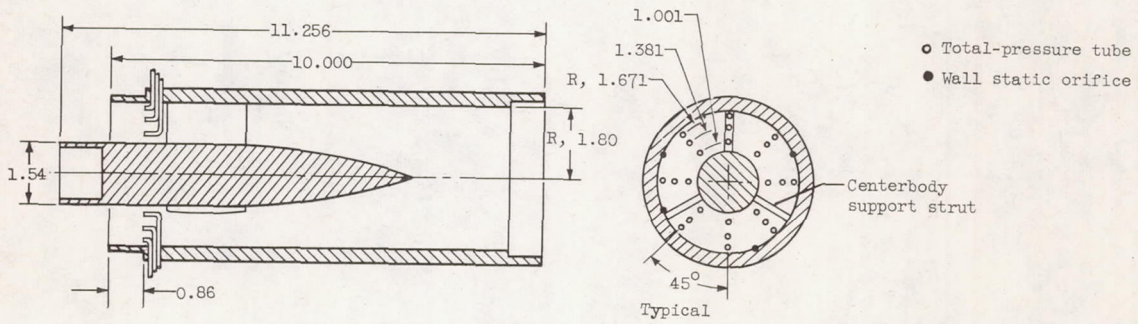


(c) Model 4-C.

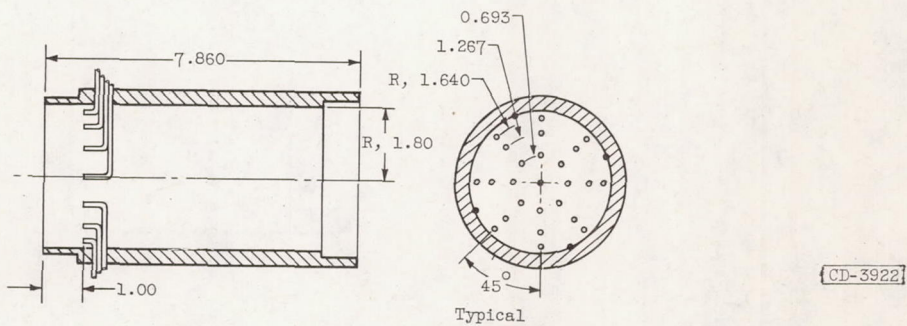
Figure 4. - Concluded. Internal area variations of curved-diffuser models.



(a) General arrangement of model and support system.



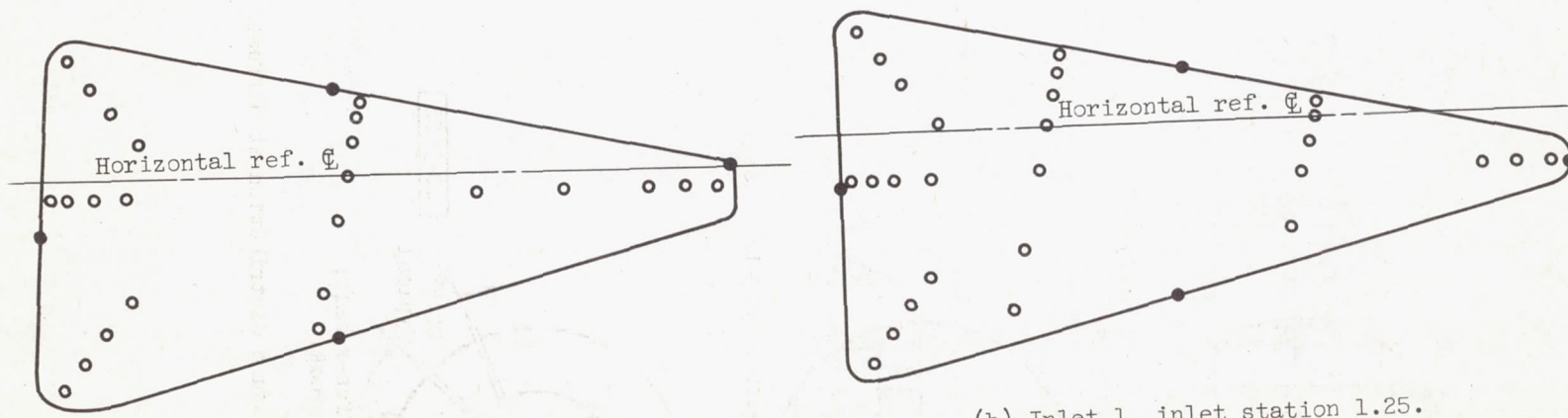
(b) Forward support body; curved-diffuser models.



(c) Forward support body; straight-diffuser models.

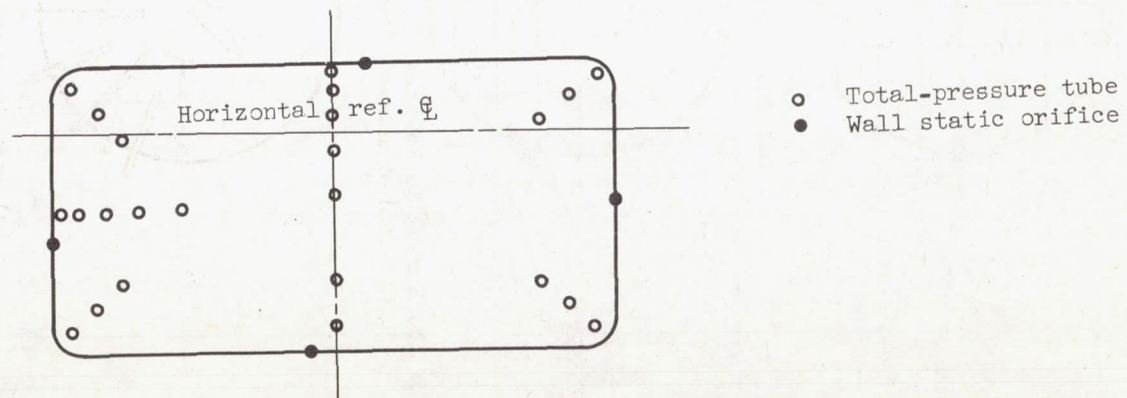
Figure 5. - Model arrangement and instrumentation (all dimensions in inches).

CD-3922



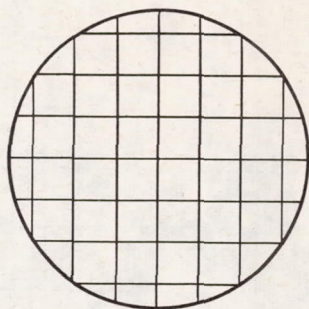
(a) Inlet 4, inlet station 1.0.

(b) Inlet 1, inlet station 1.25.

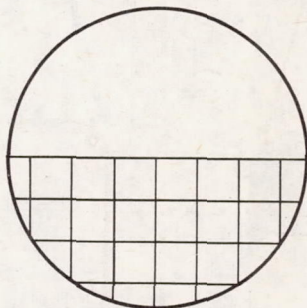


(c) Inlet 3, inlet station 1.0.

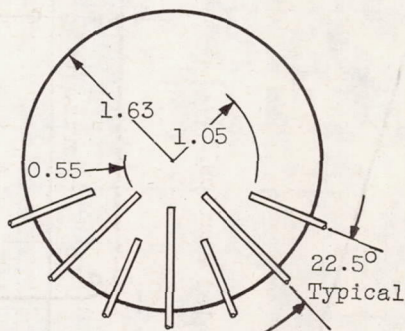
Figure 6. - Instrumentation at inlet throat.



(a) Full screen; 0.50-inch mesh, 0.051-inch-diameter wire.

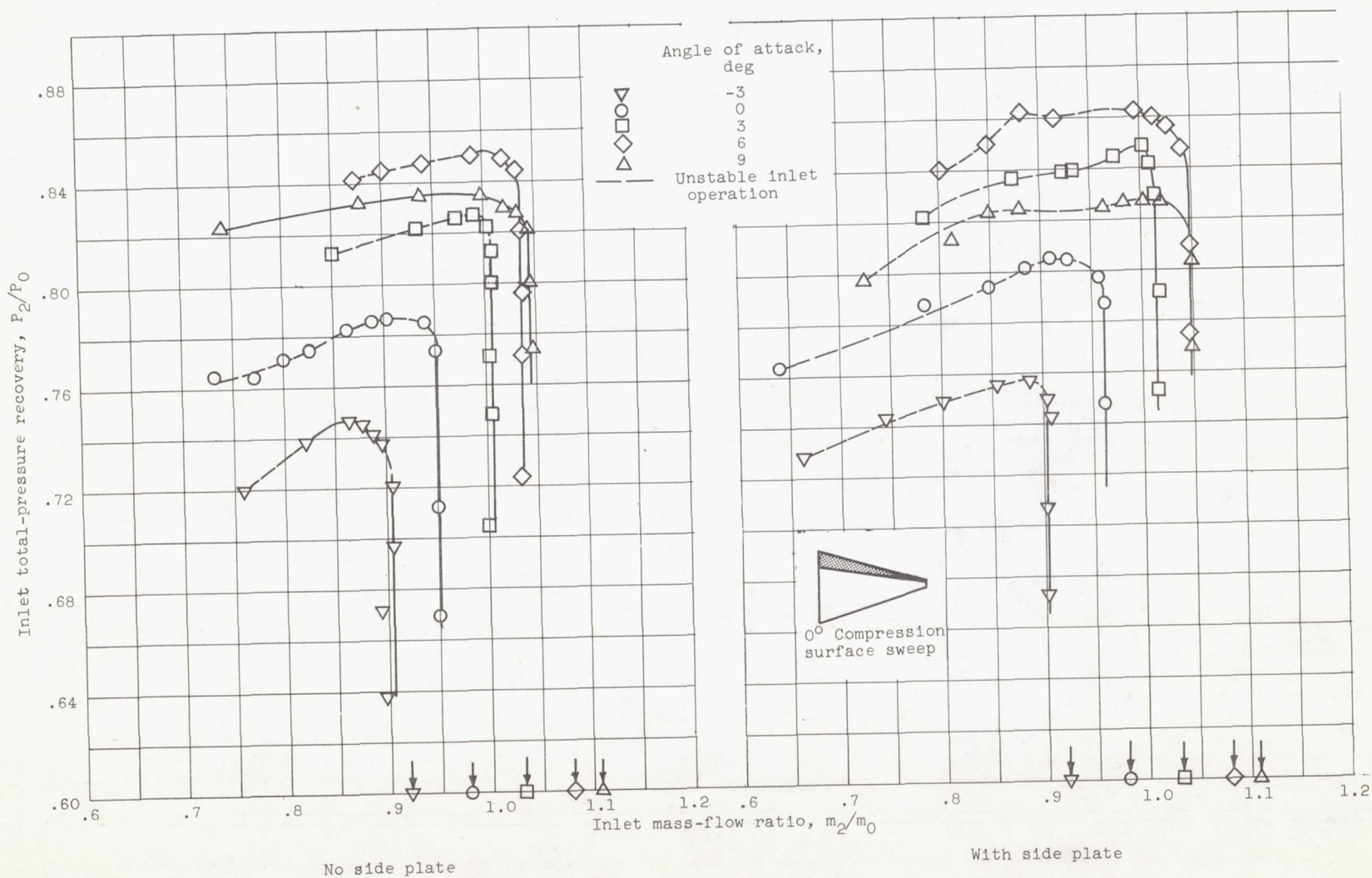


(b) Screen in lower diffuser half; 0.50-inch mesh, 0.051-inch-diameter wire.



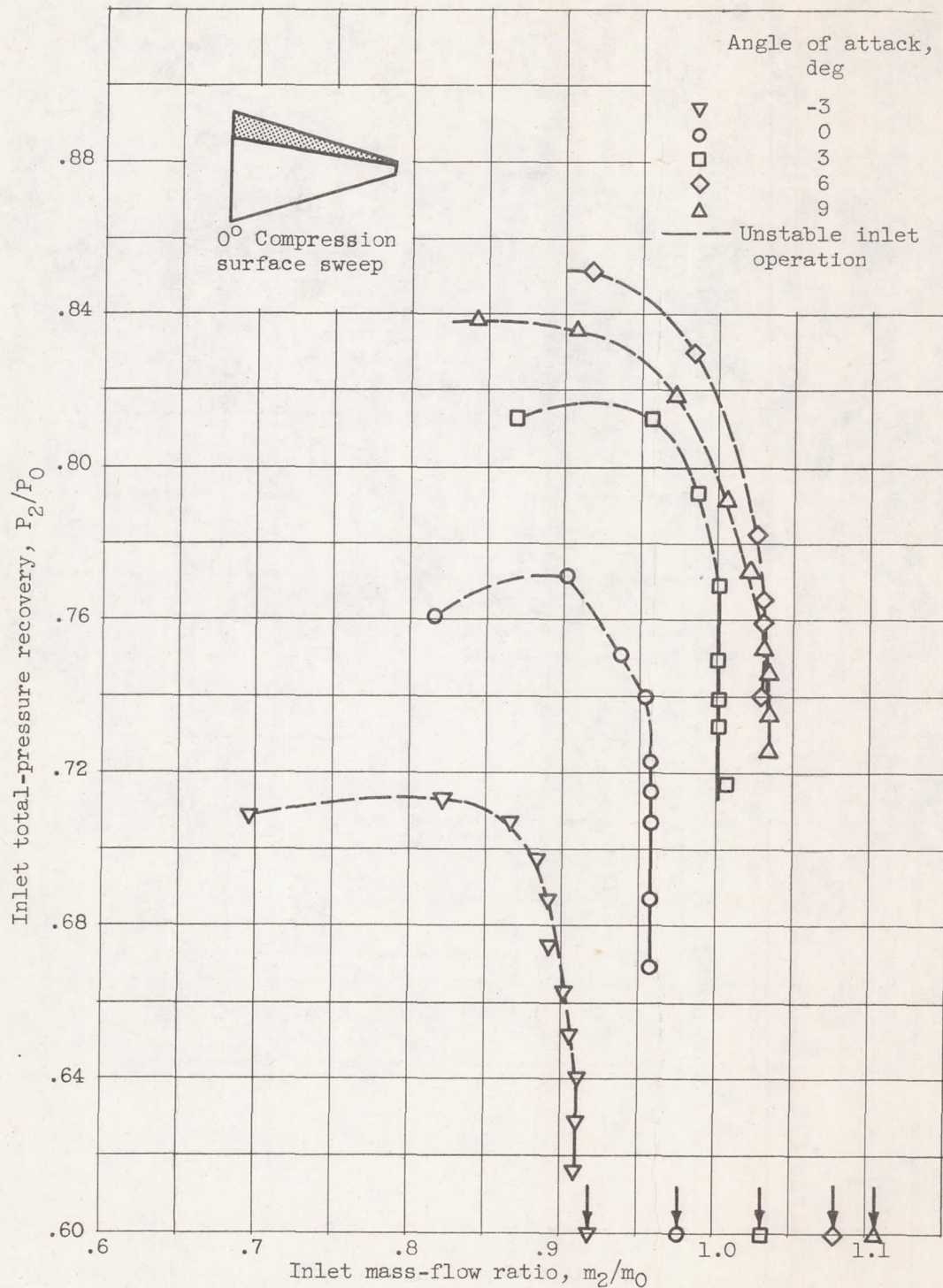
(c) Rods in lower diffuser half; 0.125-inch-diameter rods.

Figure 7. - Systems for control of total-pressure distribution at diffuser exit. Model 3-S.



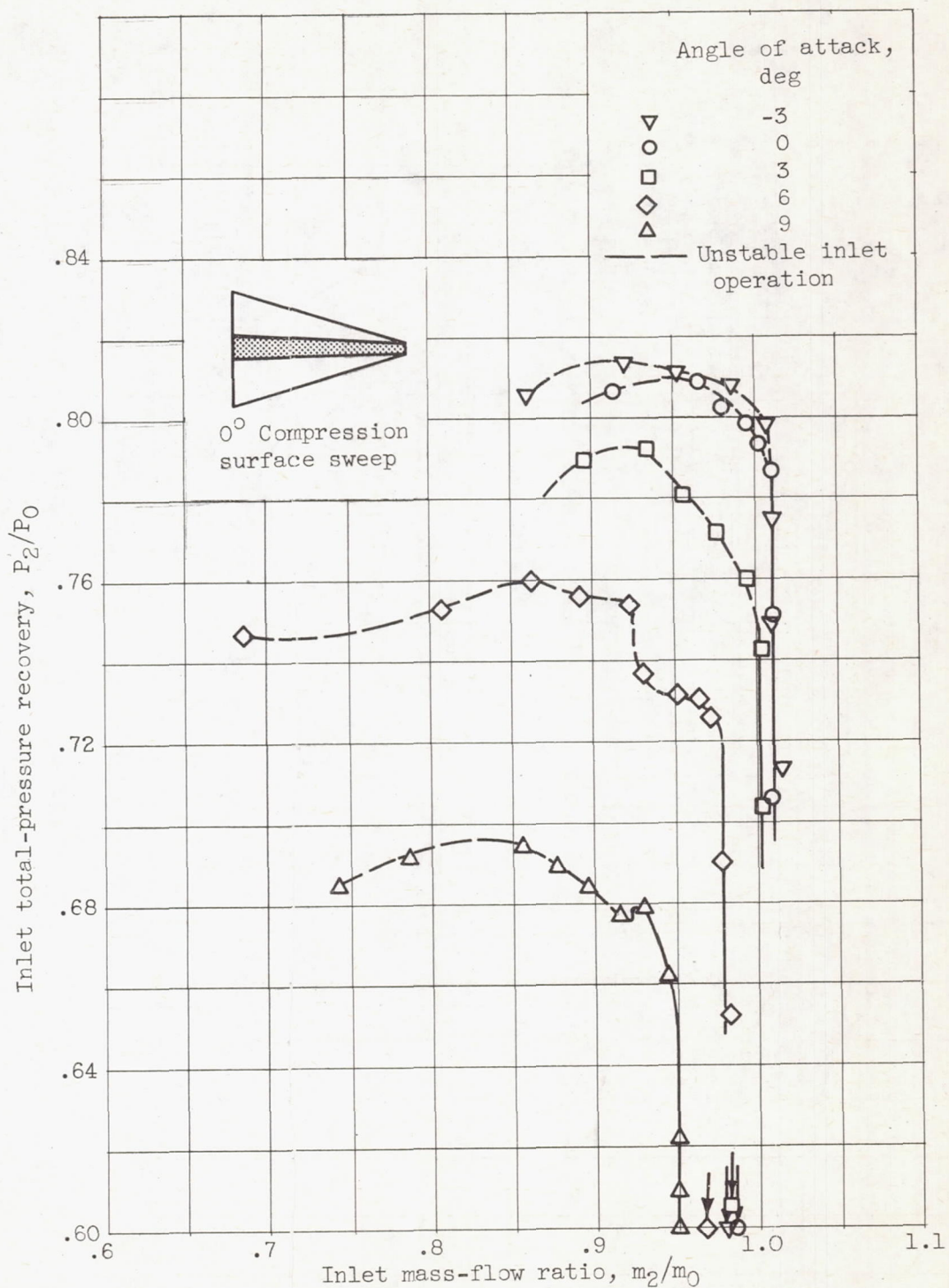
(a) Model 1-S. (Arrows on abscissa indicate theoretical critical mass-flow ratios.)

Figure 8. - Inlet performance at angle of attack.



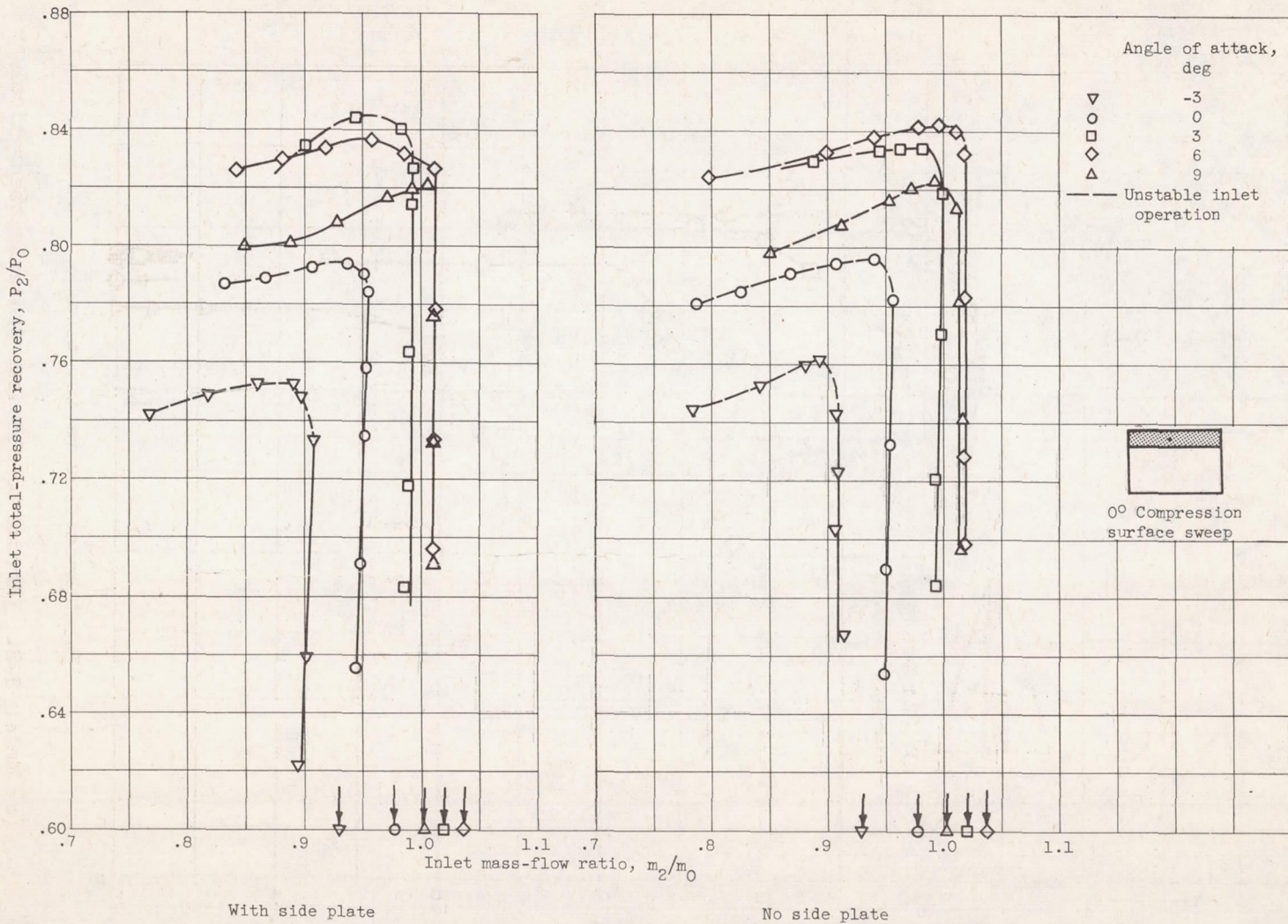
(b) Model 1-C. (Arrows on abscissa indicate theoretical critical mass-flow ratios.)

Figure 8. - Continued. Inlet performance at angle of attack.



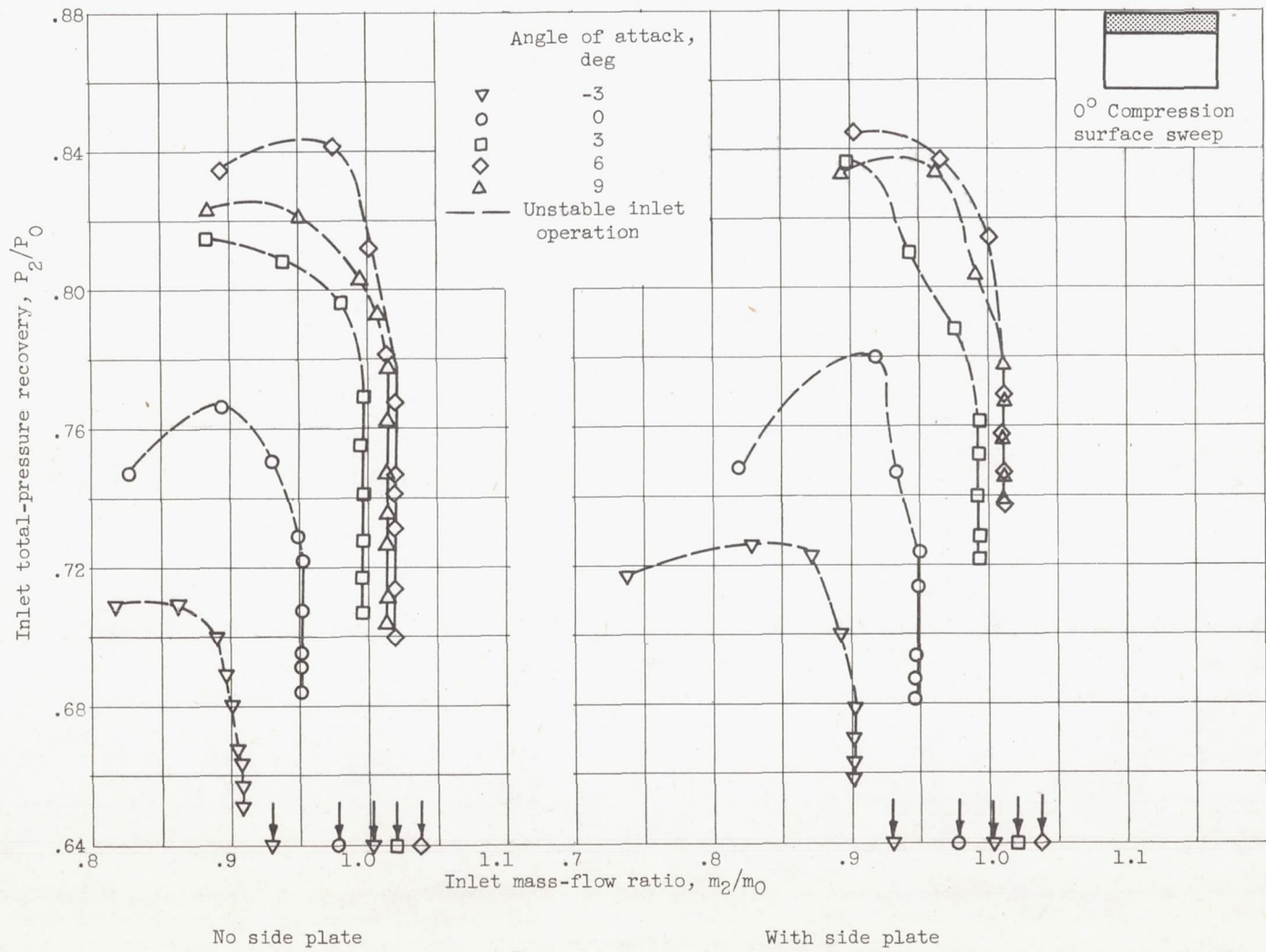
(c) Model 2-S. (Arrows on abscissa indicate theoretical critical mass-flow ratios.)

Figure 8. - (Continued. Inlet performance at angle of attack.



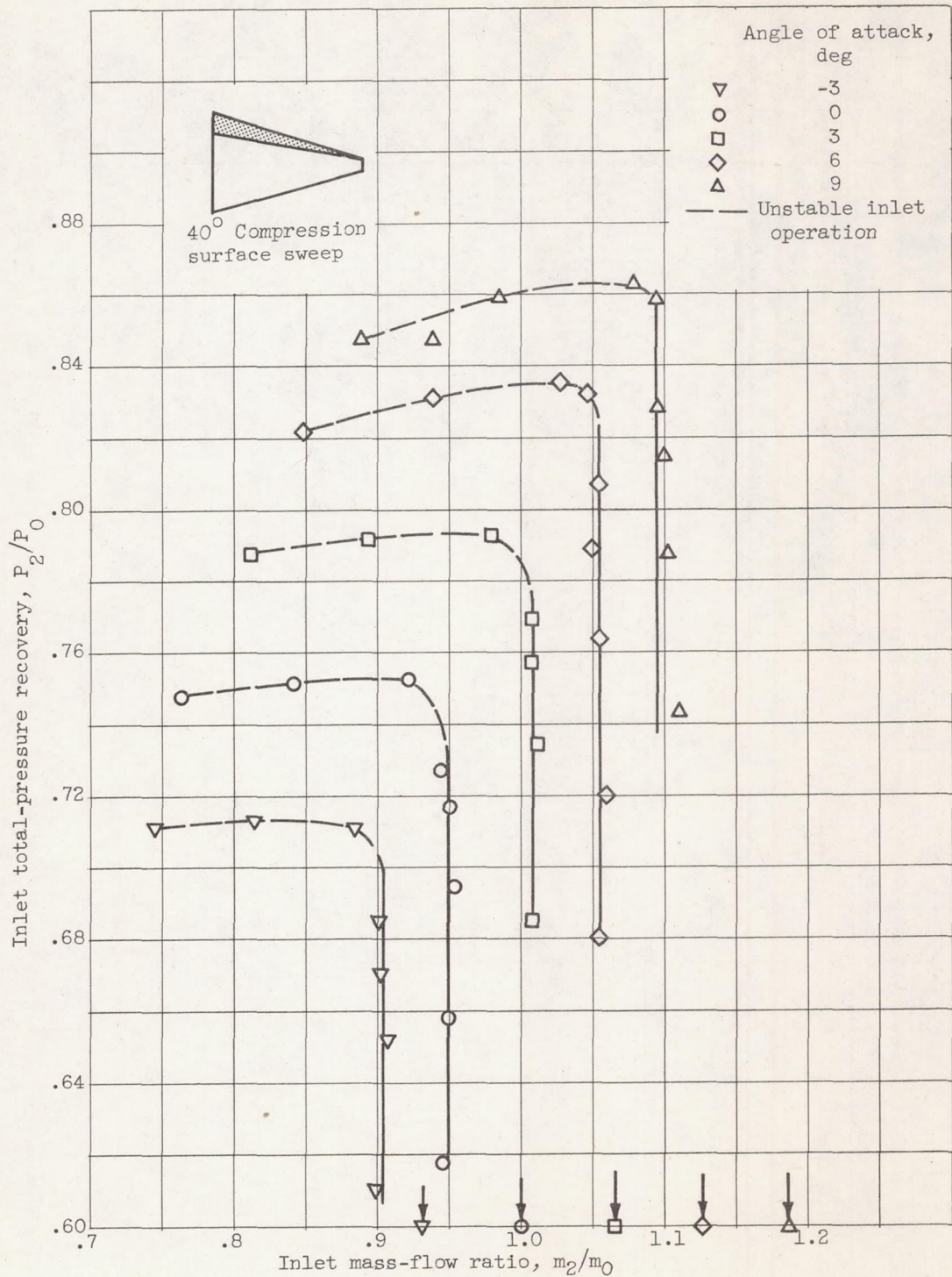
(d) Model 3-S. (Arrows on abscissa indicate theoretical critical mass-flow ratios.)

Figure 8. - Continued. Inlet performance at angle of attack.



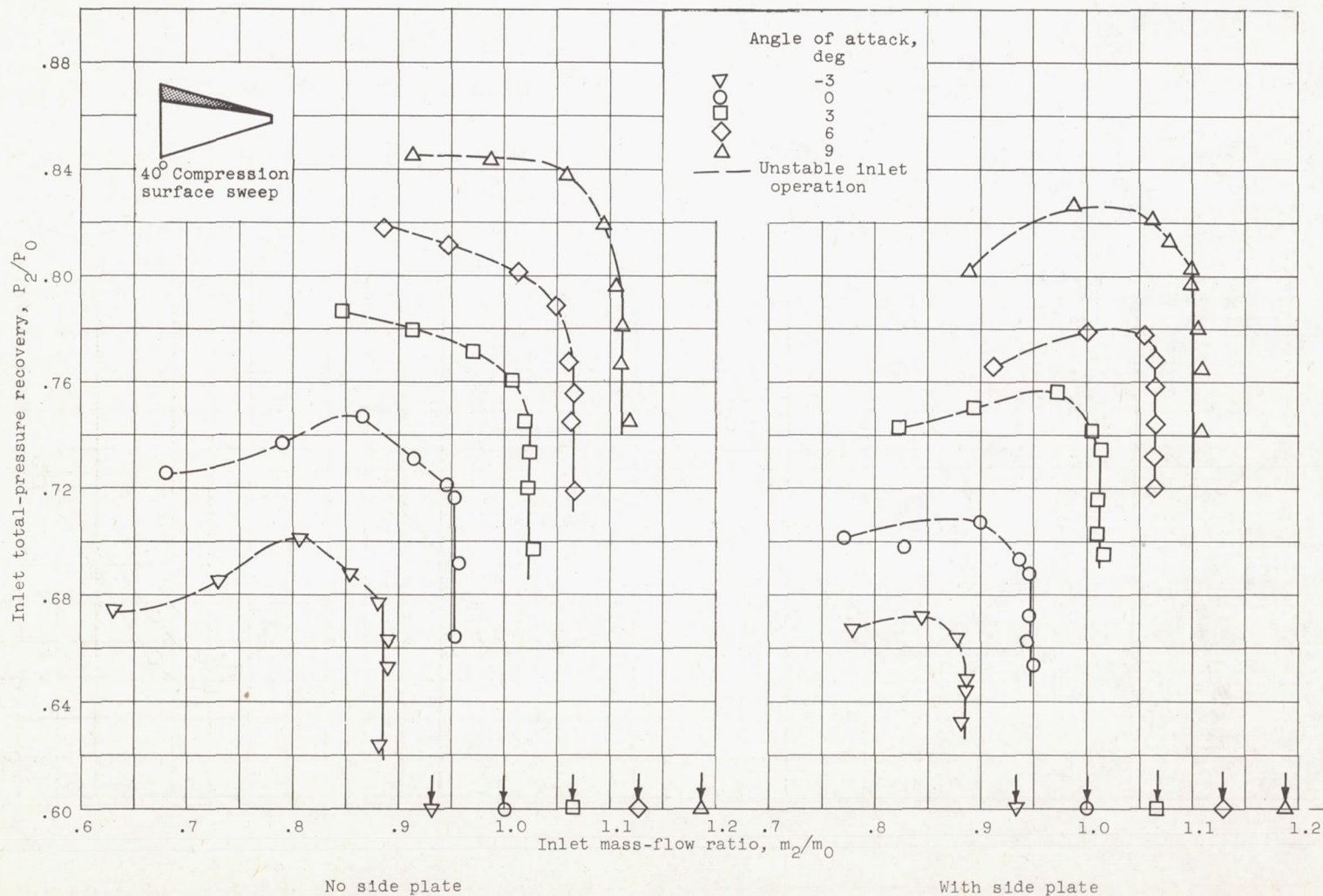
(e) Model 3-C. (Arrows on abscissa indicate theoretical critical mass-flow ratios.)

Figure 8. - Continued. Inlet performance at angle of attack.



(f) Model 4-S. (Arrows on abscissa indicate ratio of projected inlet area at angle of attack to area at zero angle of attack.)

Figure 8. - Continued. Inlet performance at angle of attack.



(g) Model 4-C. (Arrows on abscissa indicate ratio of projected inlet area at angle of attack to area at zero angle of attack.)

Figure 8. - Concluded. Inlet performance at angle of attack.

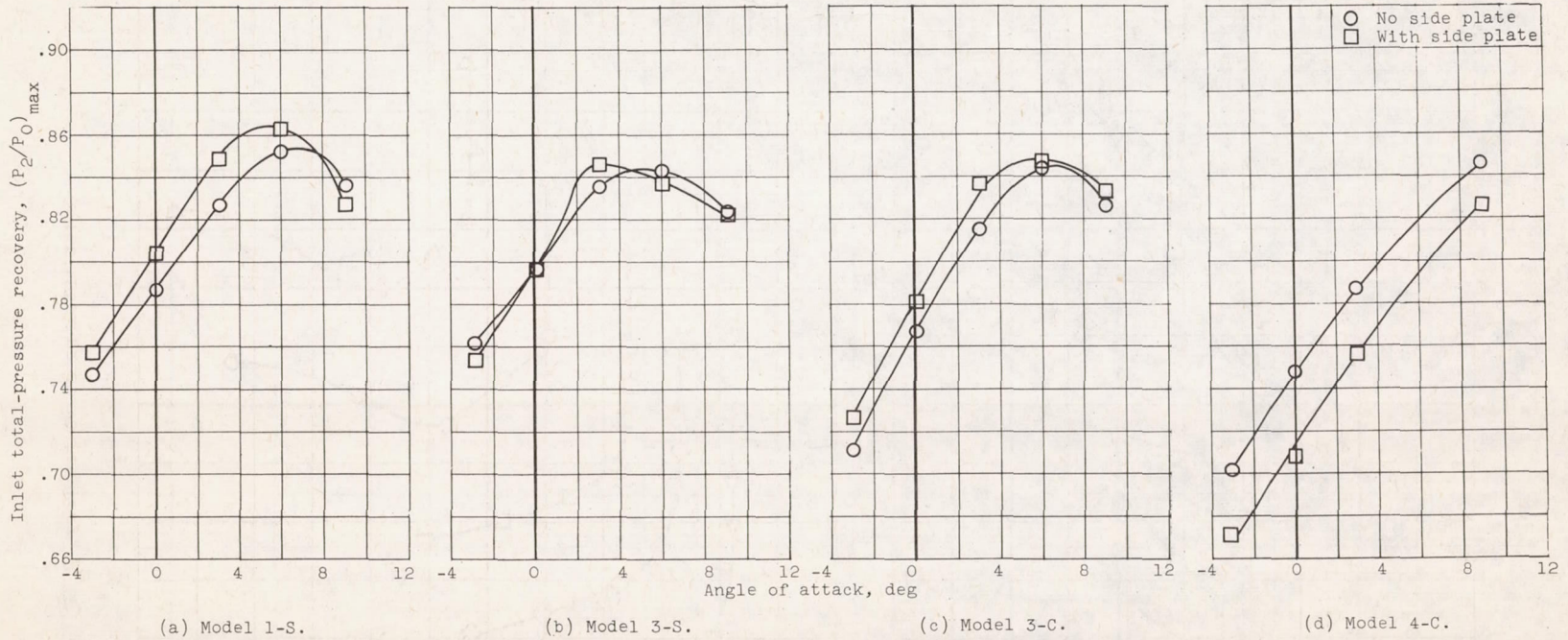


Figure 9. - Effect of side plates on inlet total-pressure recovery.

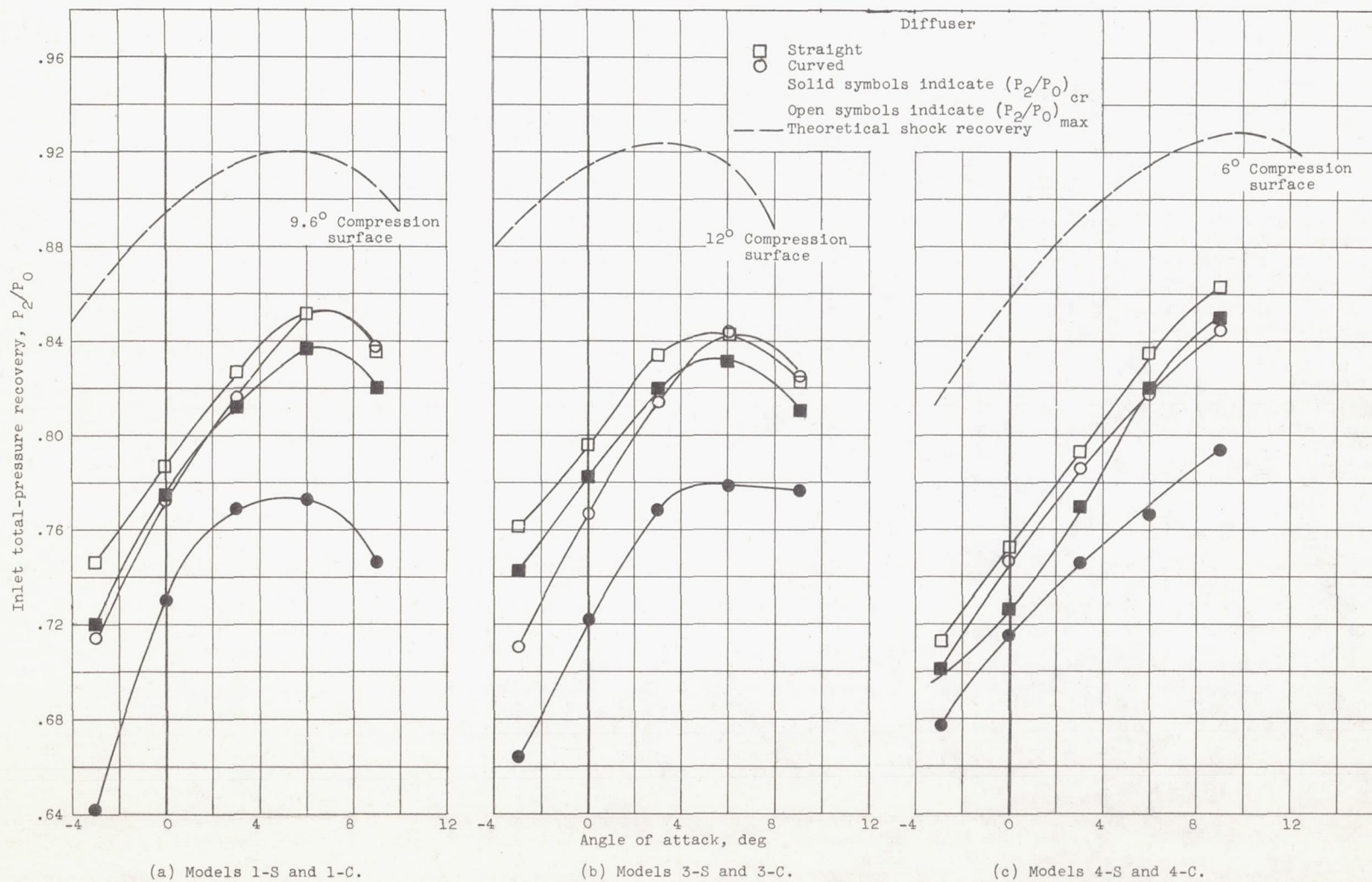
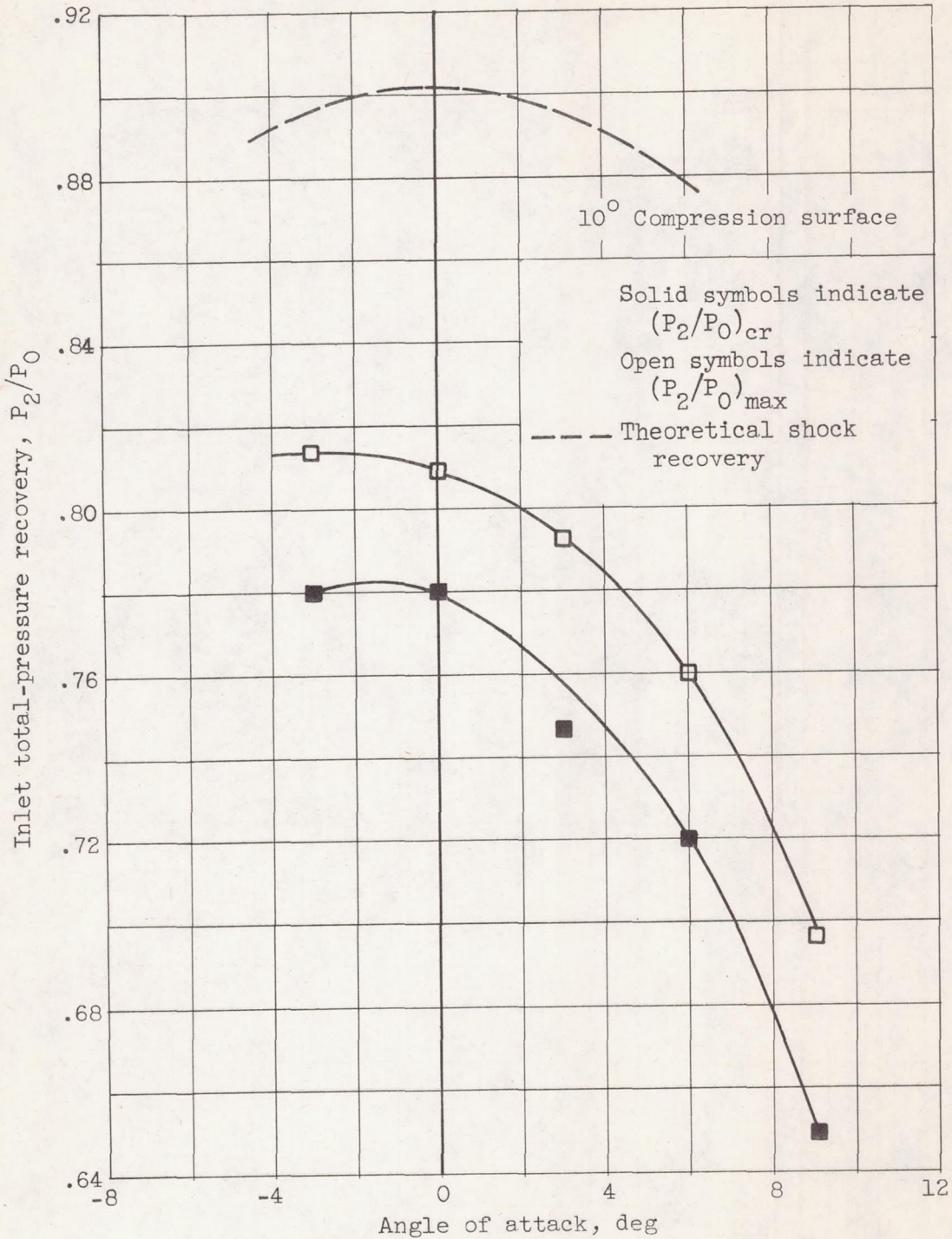
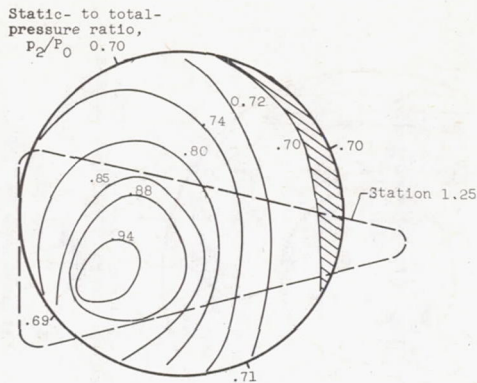


Figure 10. - Comparison of pressure-recovery performance.

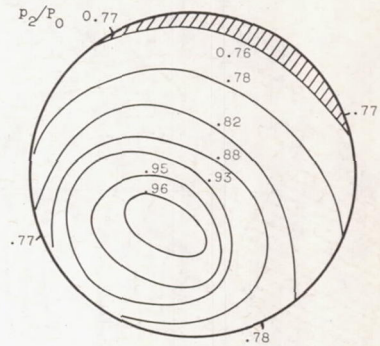


(d) Model 2-S.

Figure 10. - Concluded. Comparison of pressure-recovery performance.

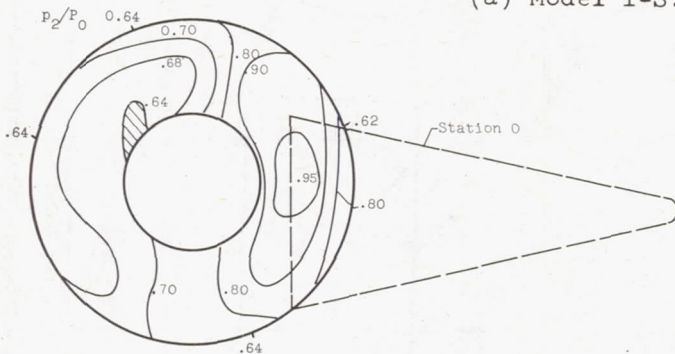


Zero angle of attack; inlet total-pressure recovery, 0.79; inlet mass-flow ratio, 0.90.

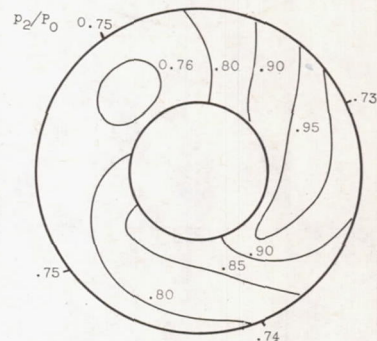


Angle of attack, 6°; inlet total-pressure recovery, 0.85; inlet mass-flow ratio, 0.99.

(a) Model 1-S.

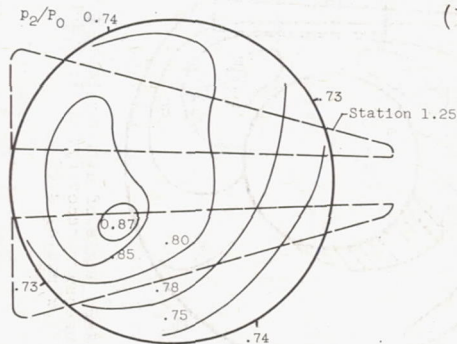


Zero angle of attack; inlet total-pressure recovery, 0.77; inlet mass-flow ratio, 0.90.

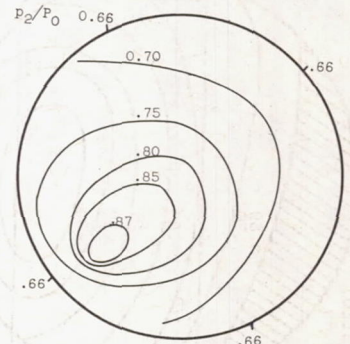


Angle of attack 6°; inlet total-pressure recovery, 0.85; inlet mass-flow ratio, 0.92.

(b) Model 1-C.



Zero angle of attack; inlet total-pressure recovery, 0.81; inlet mass-flow ratio, 0.97.

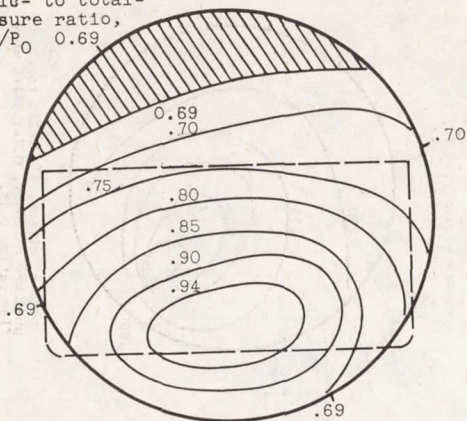


Angle of attack, 6°; inlet total-pressure recovery, 0.74; inlet mass-flow ratio, 0.93.

(c) Model 2-S.

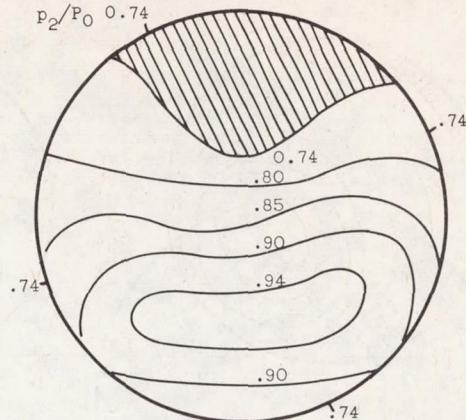
Figure 11. - Total-pressure contours at exit-rake station.

Static- to total-
pressure ratio,
 p_2/p_0 0.69



Zero angle of attack; inlet total-
pressure recovery, 0.80; inlet mass-
flow ratio, 0.94

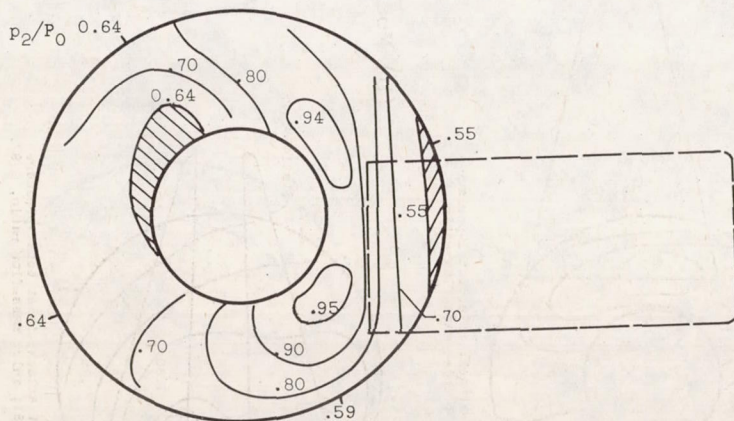
p_2/p_0 0.74



Angle of attack, 6° ; inlet total-
pressure recovery, 0.84; inlet mass-
flow ratio, 0.98.

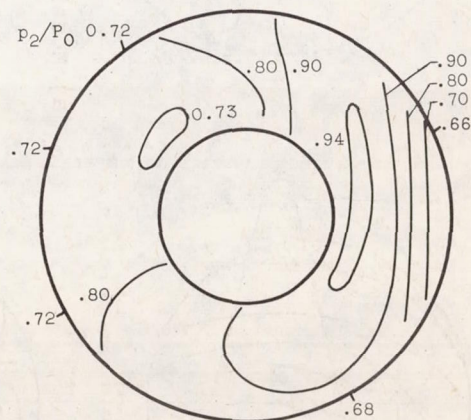
(d) Model 3-S.

p_2/p_0 0.64



Zero angle of attack; inlet total-
pressure recovery, 0.77; inlet mass-
flow ratio, 0.89.

p_2/p_0 0.72

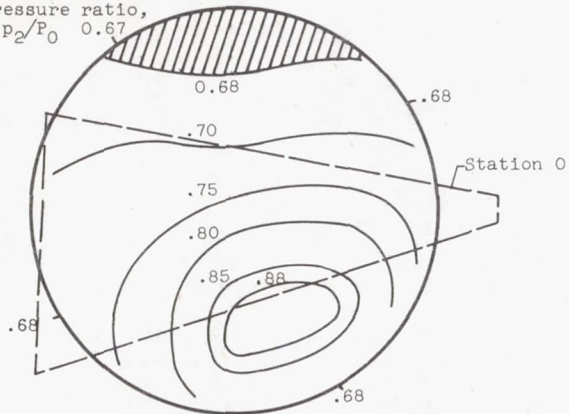


Angle of attack, 6° ; inlet total-
pressure recovery, 0.84; inlet mass-
flow ratio, 0.98.

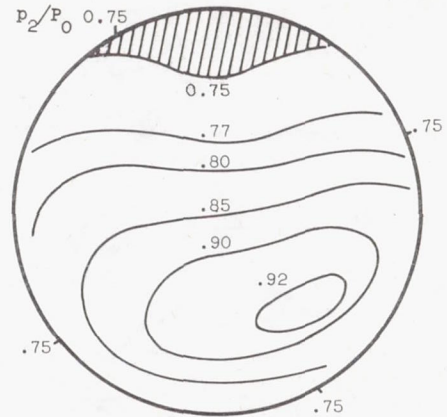
(e) Model 3-C.

Figure 11. - Continued. Total-pressure contours at exit-rake station.

Static- to total-
pressure ratio,
 p_2/P_0 0.67

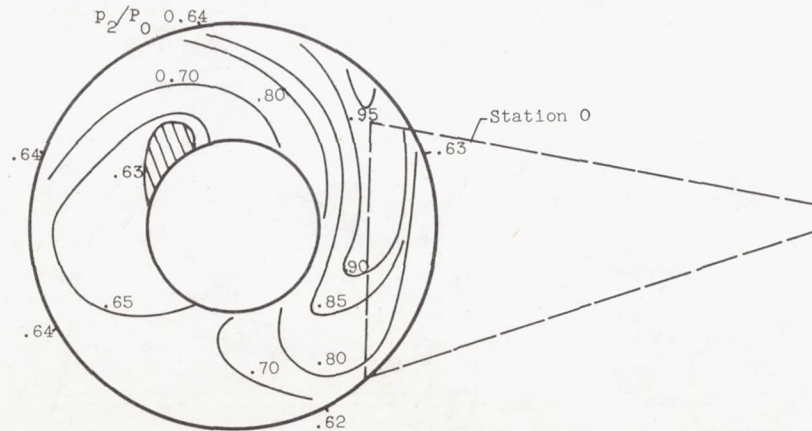


Zero angle of attack; inlet total-pressure
recovery, 0.75; inlet mass-flow ratio, 0.84.

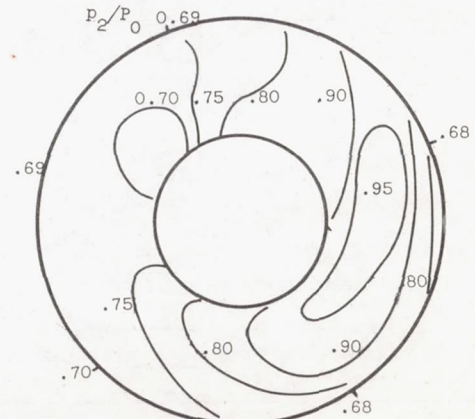


Angle of attack, 6° ; inlet total-
pressure recovery, 0.83; inlet mass-
flow ratio, 0.94.

(f) Model 4-S.



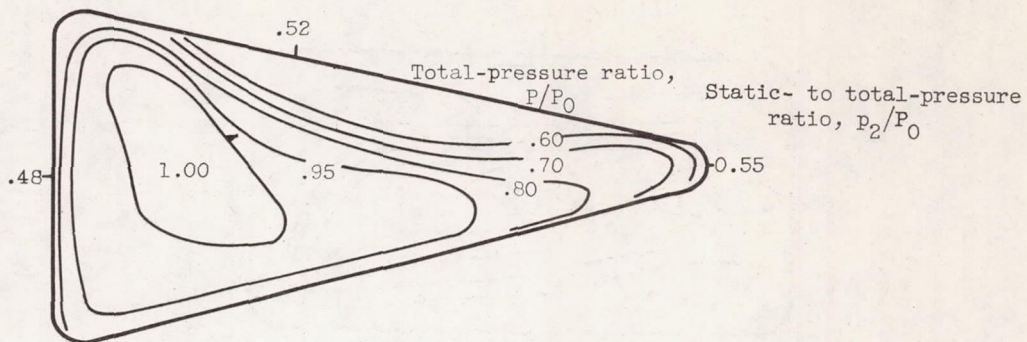
Zero angle of attack; inlet total-pressure
recovery, 0.75; inlet mass-flow ratio, 0.90.



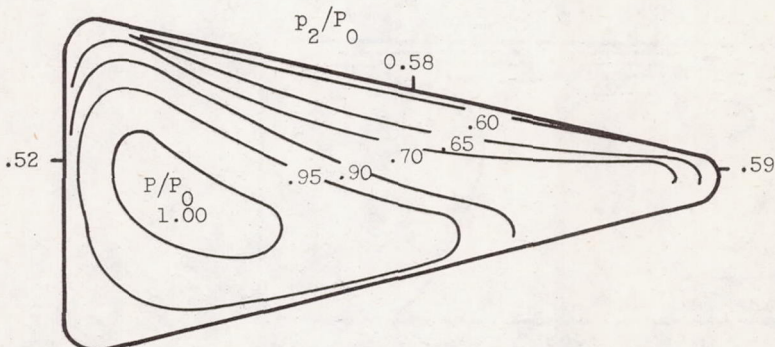
Angle of attack, 6° ; inlet total-
pressure recovery, 0.81; inlet mass-
flow ratio, 0.95.

(g) Model 4-C.

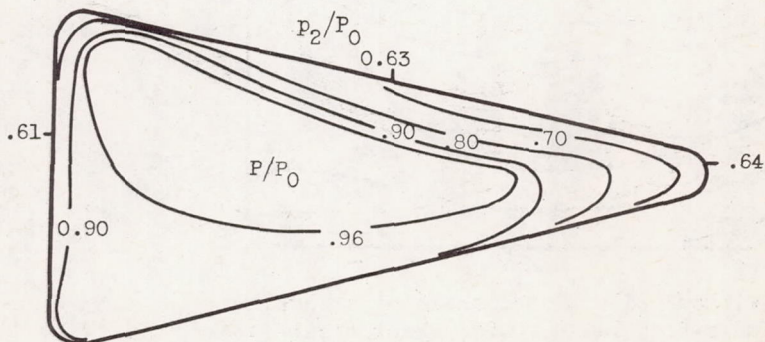
Figure 11. - Concluded. Total-pressure contours at exit-rake station.



Inlet without side plate; zero angle of attack; inlet mass-flow ratio, 0.92; theoretical shock pressure recovery, 0.89.



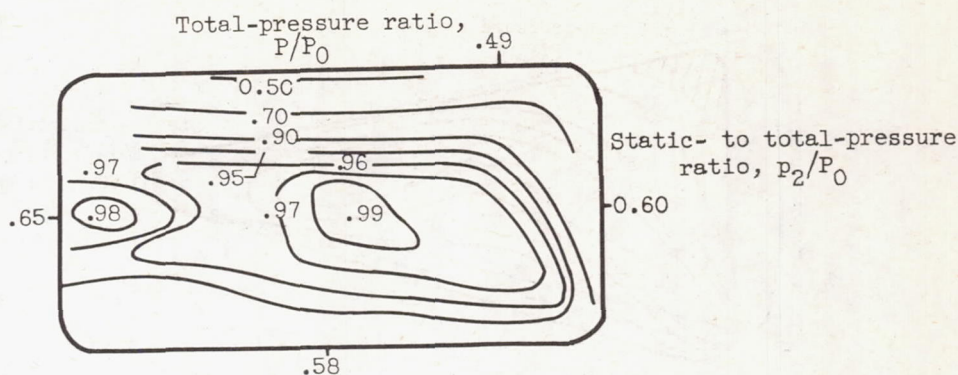
Inlet with side plate; zero angle of attack; inlet mass-flow ratio, 0.91; theoretical shock pressure recovery, 0.89.



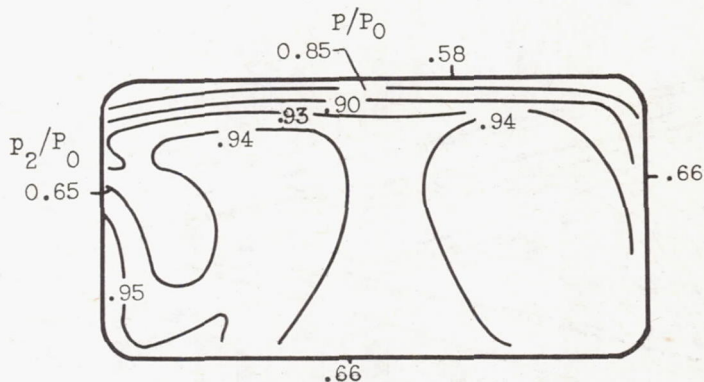
Inlet without side plate; angle of attack, 6° ; inlet mass-flow ratio, 1.00; theoretical shock pressure recovery, 0.92.

(a) Inlet 1.

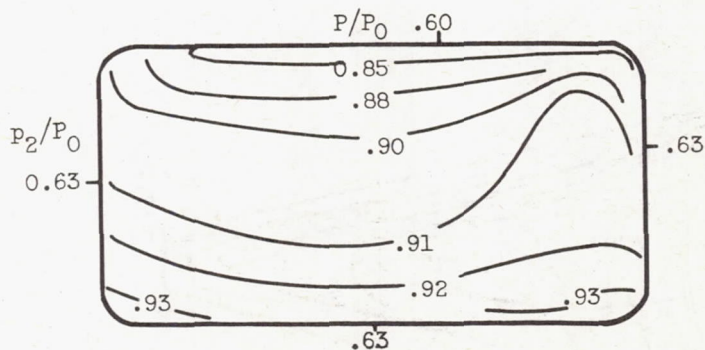
Figure 12. - Total-pressure distributions at inlet throat.



Inlet without side plate; zero angle of attack;
inlet mass-flow ratio, 0.92; theoretical shock
pressure recovery, 0.92.



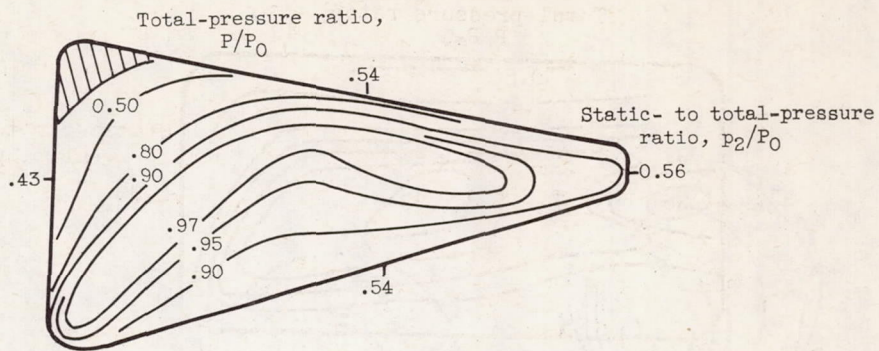
Inlet without side plate; angle of attack, 6° ;
inlet mass-flow ratio, 0.99; theoretical shock
pressure recovery, 0.92.



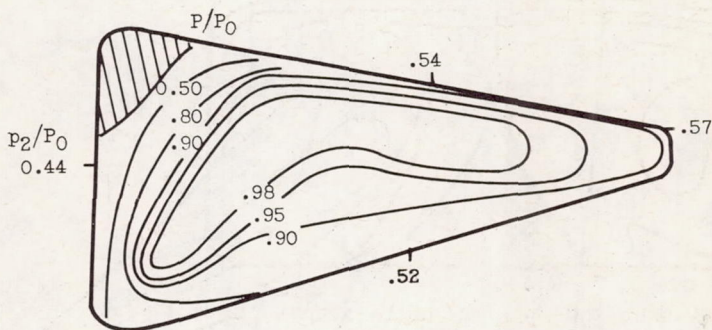
Inlet without side plate; angle of attack, 9° ;
inlet mass-flow ratio, 0.99; theoretical shock
pressure recovery, 0.86.

(b) Inlet 3.

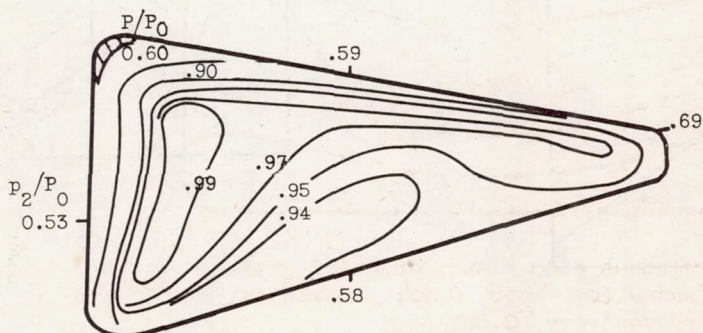
Figure 12. - Continued. Total-pressure distributions at inlet throat.



Inlet without side plate; zero angle of attack; inlet mass-flow ratio, 0.92; theoretical shock pressure recovery, 0.86.



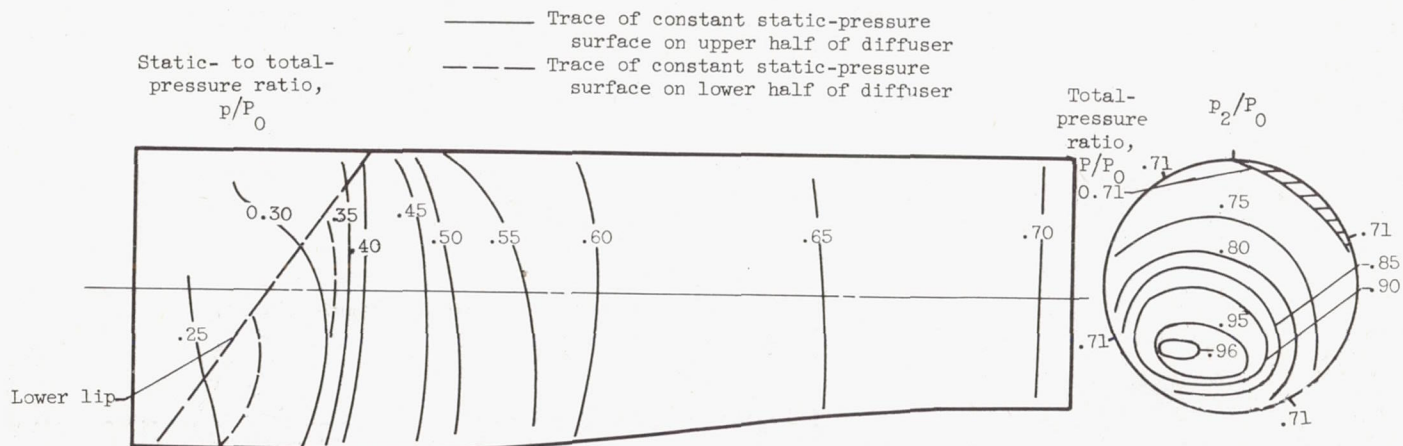
Inlet with side plate; zero angle of attack; inlet mass-flow ratio, 0.92; theoretical shock pressure recovery, 0.86.



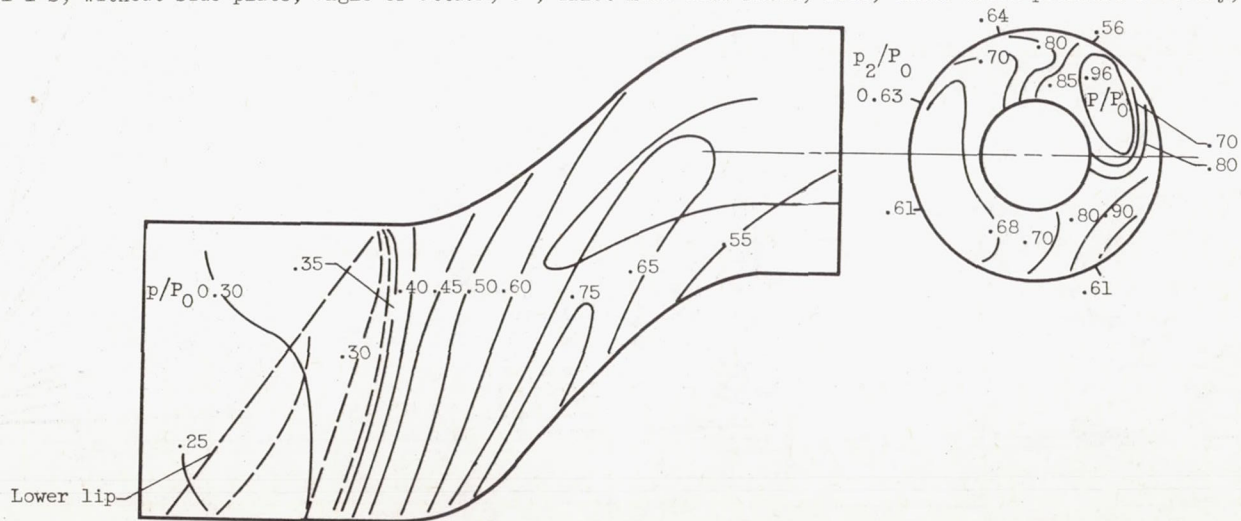
Inlet without side plate; angle of attack, 6° ; inlet mass-flow ratio, 1.03; theoretical shock pressure recovery, 0.92.

(c) Inlet 4.

Figure 12. - Concluded. Total-pressure distributions at inlet throat.

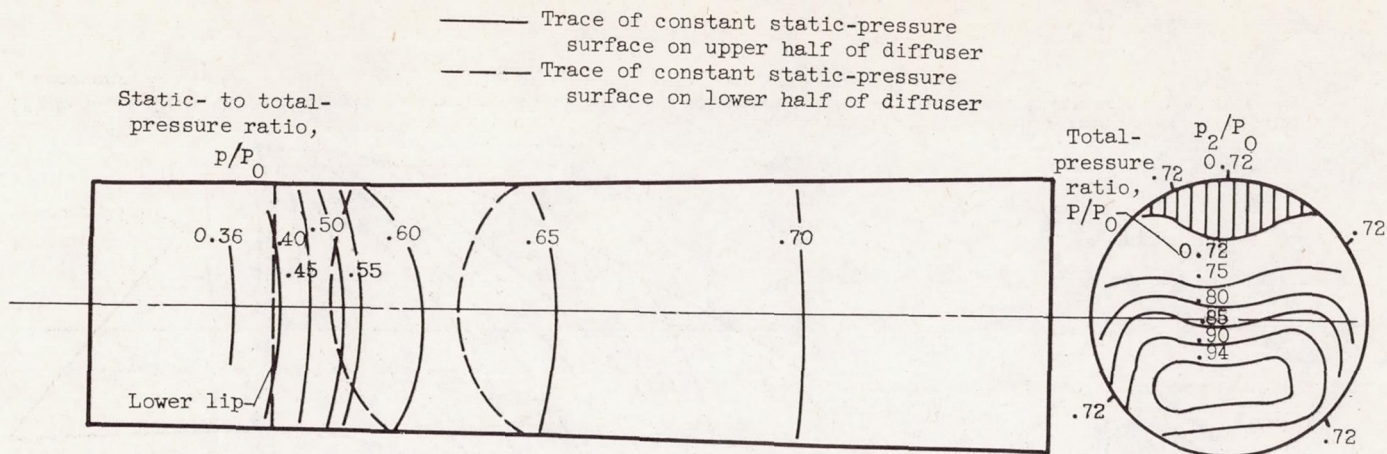


(a) Model 1-S, without side plate; angle of attack, 3° ; inlet mass-flow ratio, 1.01; inlet total-pressure recovery, 0.81.

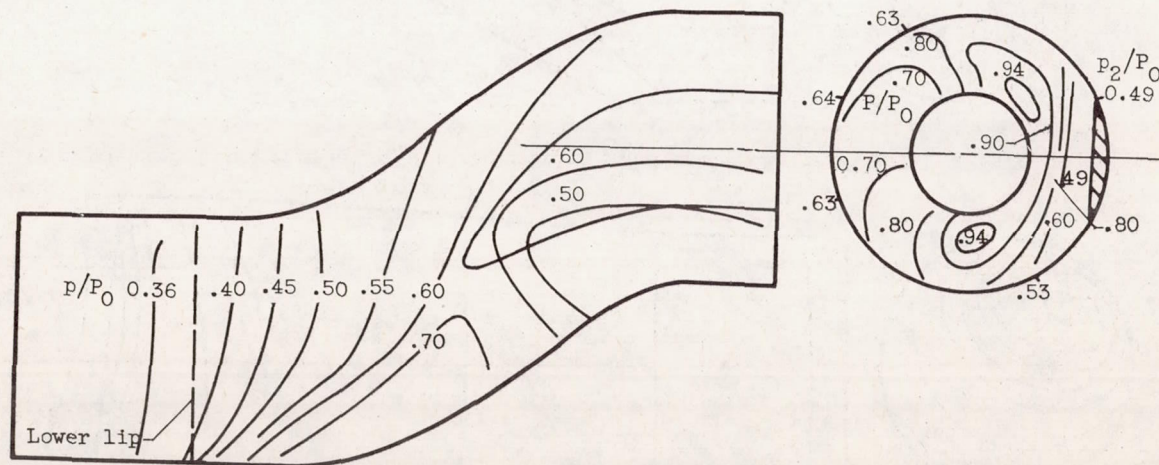


(b) Model 1-C, without side plate; angle of attack, 3° ; inlet mass-flow ratio, 1.00; inlet total-pressure recovery, 0.77.

Figure 13. - Typical internal static-pressure distributions.

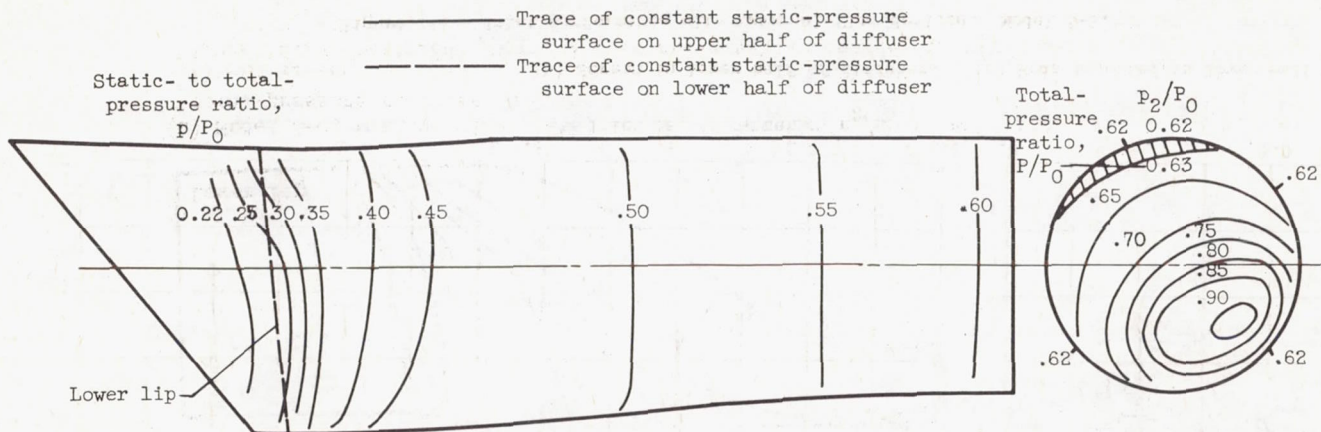


(c) Model 3-S, without side plate; angle of attack, 6° ; inlet mass-flow ratio, 1.02; inlet total-pressure recovery, 0.83.

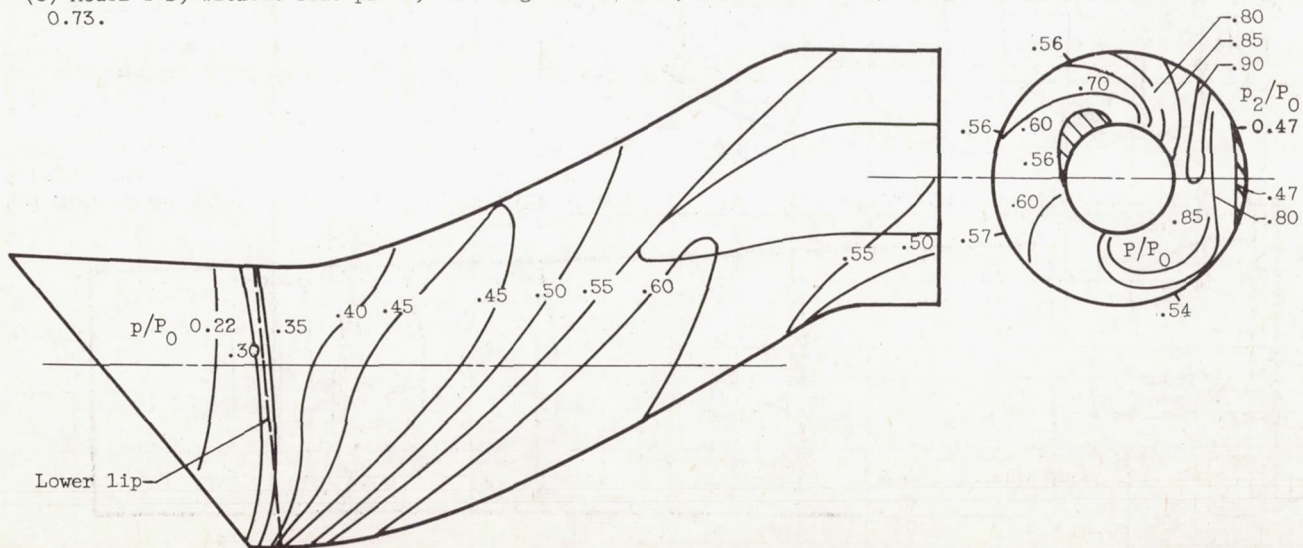


(d) Model 3-C, without side plate; angle of attack, 6° ; inlet mass-flow ratio, 1.01; inlet total-pressure recovery, 0.78.

Figure 13. - Continued. Typical internal static-pressure distributions.

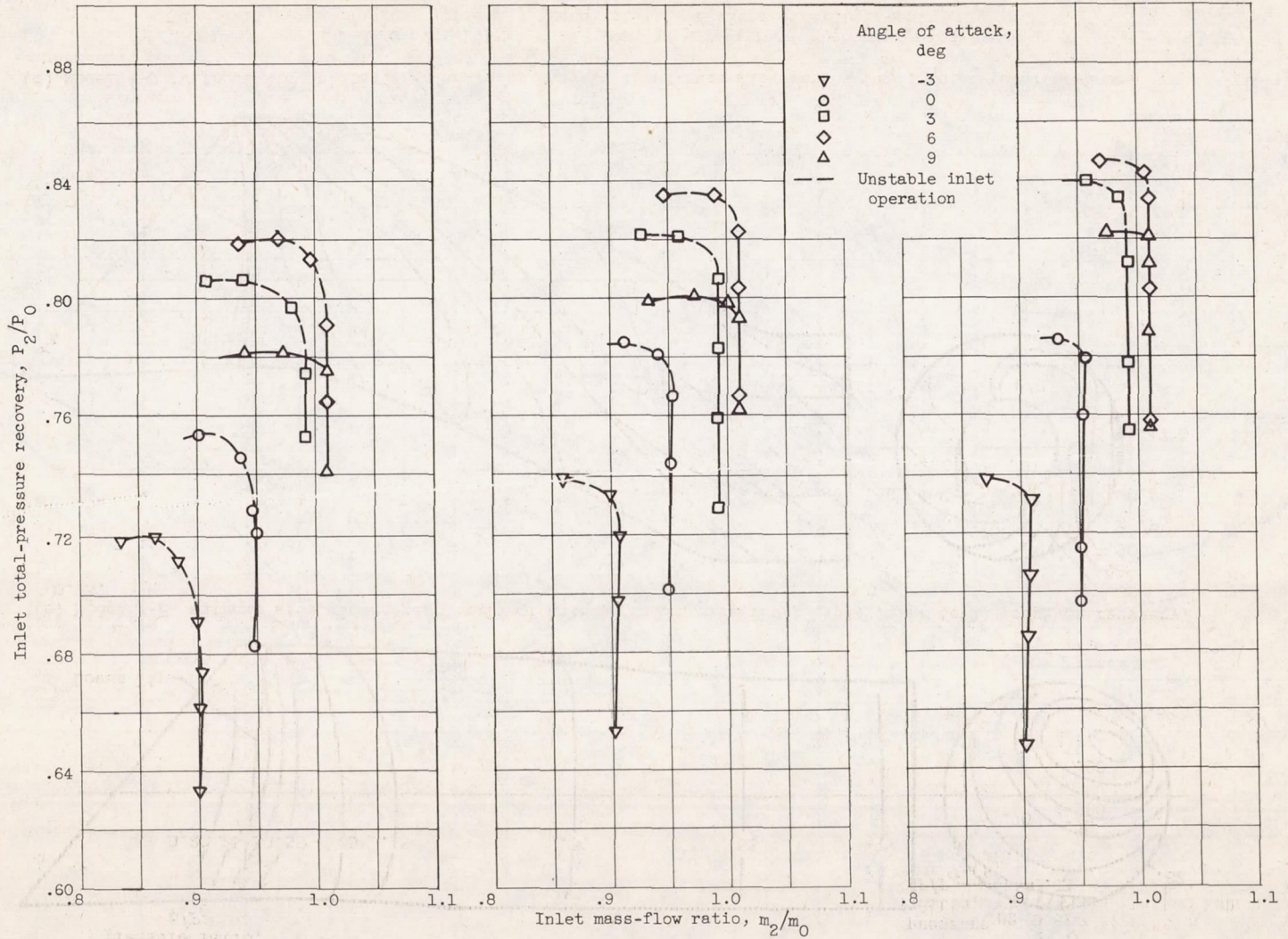


(e) Model 4-S, without side plate; zero angle of attack; inlet mass-flow, 0.94; inlet total-pressure recovery, 0.73.



(f) Model 4-C, without side plate; zero angle of attack; inlet mass-flow ratio, 0.95; inlet total-pressure recovery, 0.72.

Figure 13. - Concluded. Typical internal static-pressure distributions.



(a) Full screen. (b) Screen in lower half of diffuser. (c) Rods inserted in lower half of diffuser.

Figure 14. - Inlet performance with internal-flow devices. Model 3-S.

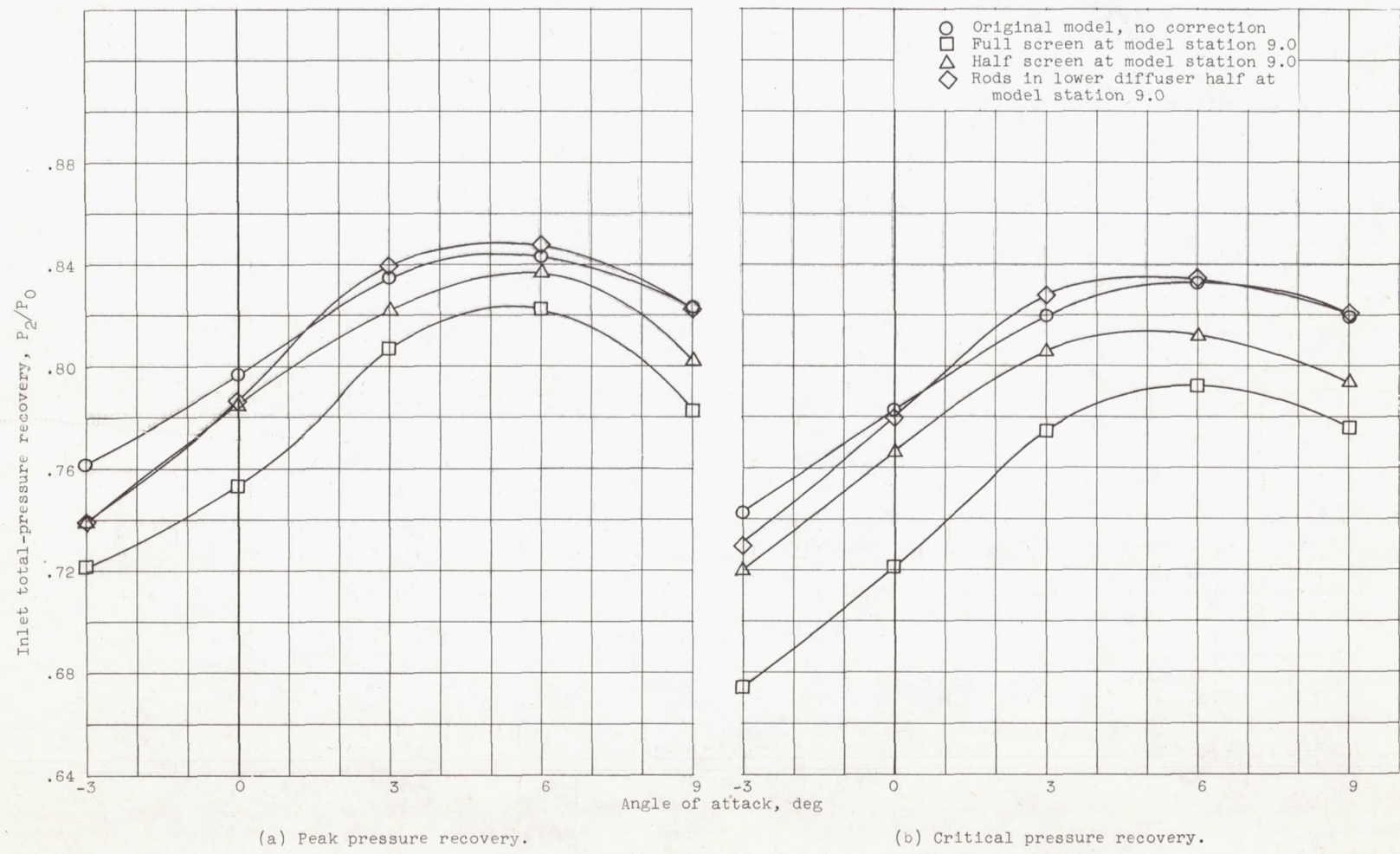


Figure 15. - Effect of internal-flow control devices on pressure recovery of model 3-S. No side plate.

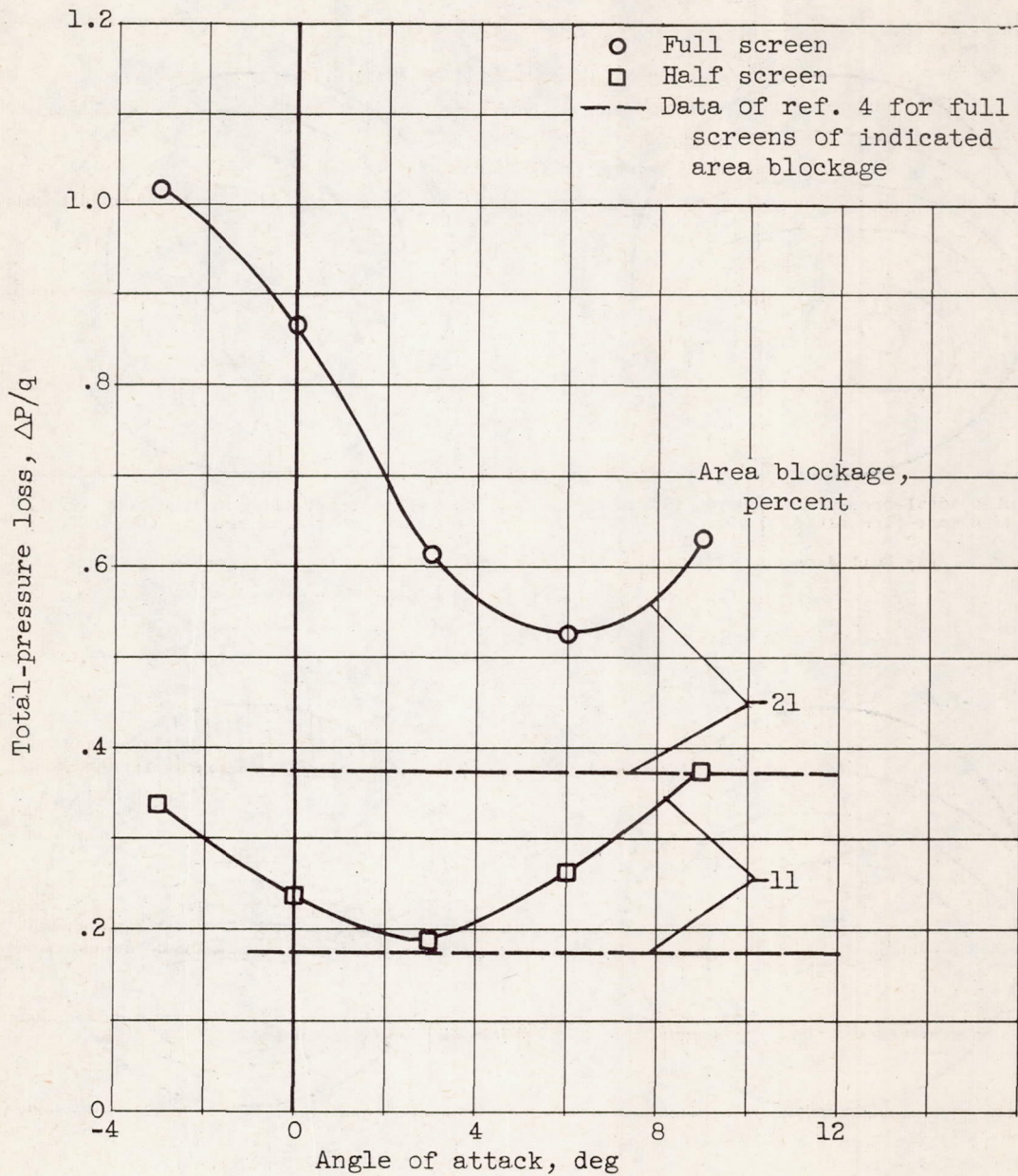
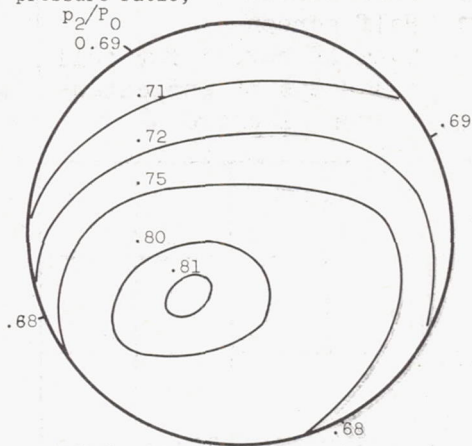


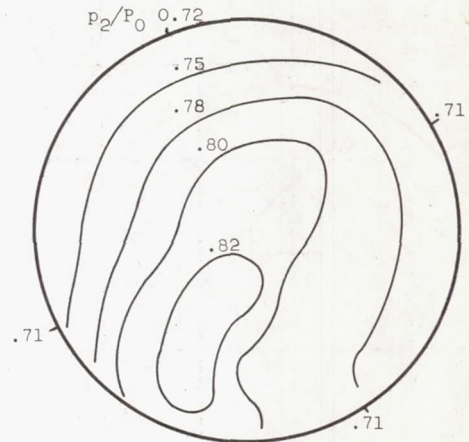
Figure 16. - Total-pressure loss across screens for internal flow control.

Static- to total-
pressure ratio,



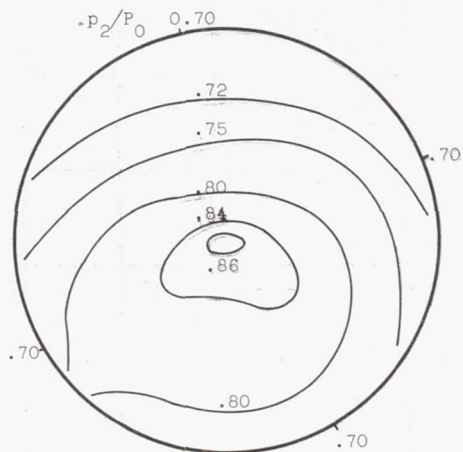
Inlet total-pressure recovery, 0.75;
inlet mass-flow ratio, 0.90.

(a) Full screen.



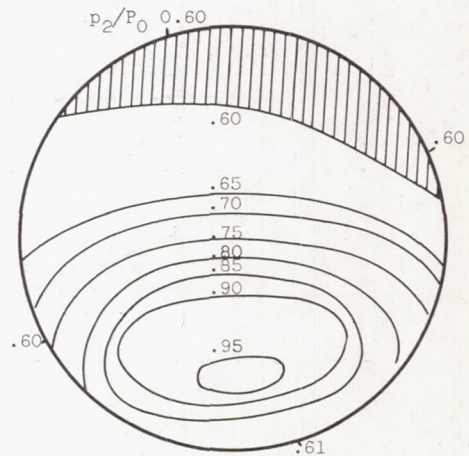
Inlet total-pressure recovery, 0.78;
inlet mass-flow ratio, 0.94.

(b) Half screen.



Inlet total-pressure recovery, 0.78;
inlet mass-flow ratio, 0.96.

(c) Rods in lower half.



Inlet total-pressure recovery, 0.73;
inlet mass-flow ratio, 0.95.

(d) No internal-flow control devices.

Figure 17. - Effect of internal-flow control devices on exit total-pressure contours. Model 3-S; zero angle of attack.

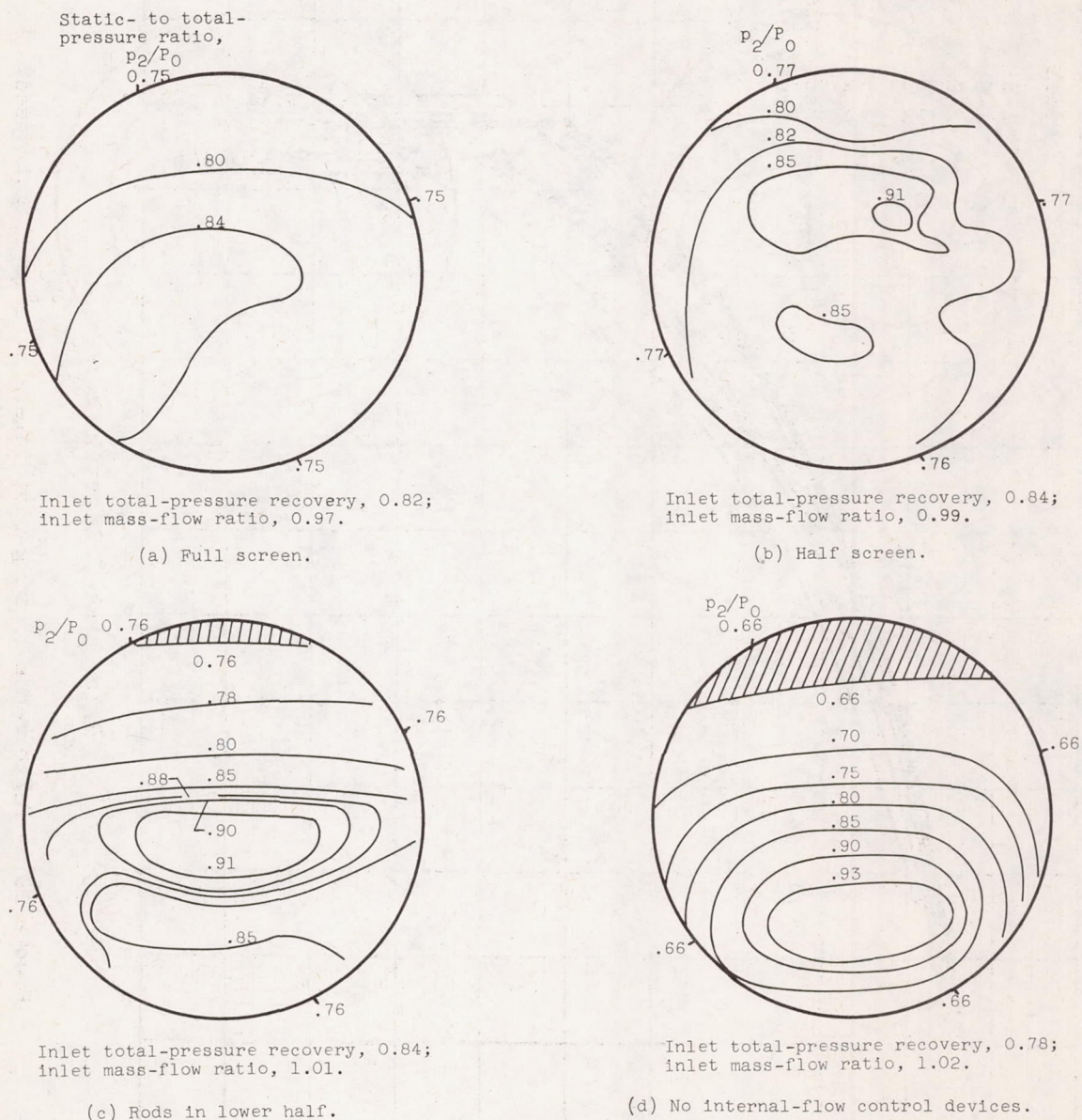


Figure 18. - Effect of internal-flow control devices on exit total-pressure contours. Model 3-S; angle of attack, 6° .

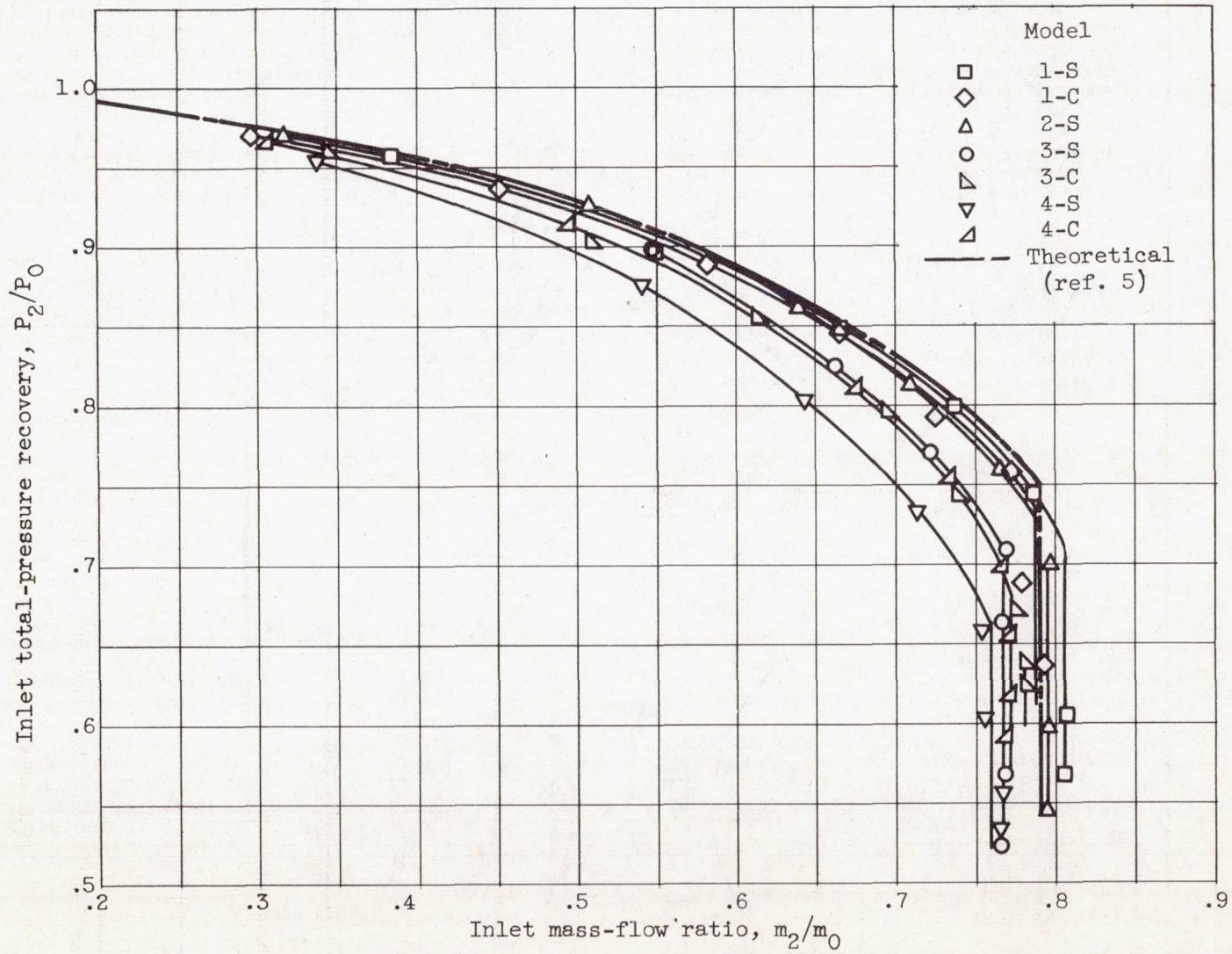


Figure 19. - Performance of wing-root inlets at zero flight speed.